Geophysical Journal International

Geophys. J. Int. (2012) doi: 10.1111/j.1365-246X.2012.05423.x

The structure of the crust and uppermost mantle beneath South China from ambient noise and earthquake tomography

Longquan Zhou,[1] Jiayi Xie,[2] Weisen Shen,[2] Yong Zheng,[3] Yingjie Yang,[4] Haixia Shi[1] and Michael H. Ritzwoller[2]

[1] *China Earthquake Network Center, China Earthquake Administration, Beijing,* 100045 *China. E-mail: lqzhou@seis.ac.cn*
[2] *Department of Physics, Center for Imaging the Earth's Interior, University of Colorado at Boulder, Boulder, CO* 80309*, USA*
[3] *State Key Laboratory of Geodesy and Earth's Dynamics, Institute of Geodesy and Geophysics, CAS, Wuhan, China*
[4] *Department of Earth and Planetary Sciences, Macquarie University,* 2109 *Sydney, Australia*

Accepted 2012 February 22. Received 2012 February 22; in original form 2011 September 8

SUMMARY

Two years of continuous recordings of ambient seismic noise observed at 354 stations in South China from 2009 to 2010 are used to estimate Rayleigh wave group and phase velocity maps from 6 to 40 s period. These results are merged with Rayleigh wave phase velocity maps from 25 to 70 s period derived from earthquakes in the same time frame. Eikonal tomography generates the dispersion maps, which, by Monte–Carlo inversion, are used to estimate a 3-D Vsv model of the crust and upper mantle down to a depth of 150 km across all of South China with attendant uncertainties. A clear image emerges of the 'West Yangtze Block', a region of the western Yangtze Craton characterized by relatively thick crust (∼40 km) overlying a seismic mantle lithosphere that extends to at least 150 km that may have been the nucleus for the formation of the Yangtze craton in the Archean and may present a present-day obstacle to the eastward expansion of Tibet. The West Yangtze Block contrasts with the thinner crust (∼30 km) and mantle lithosphere (∼70–80 km) beneath the eastern Yangtze Craton and South China Foldbelt. These observed differences are consistent with processes associated with flat slab subduction in the Mesozoic that may have eroded the lithosphere of the eastern Yangtze Craton and the South China Foldbelt.

Key words: Surface waves and free oscillations; Seismic tomography; Crustal structure; Asia.

1 INTRODUCTION

The recent tectonic evolution of eastern Asia (e.g. Yin 2010) has been driven by subduction to the east and continental collision to the west. Eastern China is a fairly passive participant in this neo-tectonic framework, having formed no later than the early Paleozoic. The paleo-architecture of Eastern China is dominated by two crustal blocks, the Sino-Korean (or North China) Craton and the South China Block, which are separated by the Qinling–Dabie–Sulu orogenic belt. The South China Block is the subject of this study and is believed to have formed by the collision between the Yangtze Craton and the Cathasyia Block (e.g. Zheng *et al.* 2006). The Cathasyia Block divides further into the South China Foldbelt and the younger Youjiang Block to the west (Zhang *et al.* 2003). (Fig. 1a.) The Sino-Korean and Yangtze Cratons are both Archean in age, but the geological structure of the Yangtze Craton is more poorly understood because it is largely shrouded in Proterozoic cover strata. The Yangtze Craton encompasses two large sedimentary basins, the Jianghan Basin and the Sichuan Basin, whose substructure may have served as the nucleus of formation for the Yangtze Craton (Zhang *et al.* 1984). The South China Block is tectonically stable and suffers few earthquakes, except along its northern margin and western margin where it presents an obstacle to eastern mass transport from the Tibetan Plateau (e.g. Royden *et al.* 1997) and numerous large earthquakes occur (e.g. Zhang *et al.* 2003).

A number of factors have inhibited the seismic imaging of the crust and upper mantle beneath the South China Block, including the lack of seismicity and poor station coverage historically. At least parts of the South China Block have been imaged by larger scale tomographic studies, including Ritzwoller & Levshin (1998), Ritzwoller *et al.* (1998), Teng *et al.* (2001), Villasenor *et al.* (2001), Lebedev & Nolet (2003), Huang *et al.* (2003) and Zheng *et al.* (2008). By the end of 2007, however, a new digital seismic observing system had been completed in China that was based on aggregating seismic stations from individual provincial networks (Zheng *et al.* 2010a). We refer to this as CEArray. This data resource has already been used for *P*-wave traveltime tomography (e.g. Li & van der Hilst 2010) and surface wave tomography in neighboring regions (e.g. Yang *et al.* 2010, 2011; Zheng *et al.* 2010b, 2011). CEArray in South China consists of 425 seismic stations equipped with very broad-band (VBB), ultra broad-band (UBB), or broad-band (BB) seismometers (Fig. 1b).

We present here a new step in imaging the crust and uppermost mantle beneath the South China Block: Rayleigh wave tomography

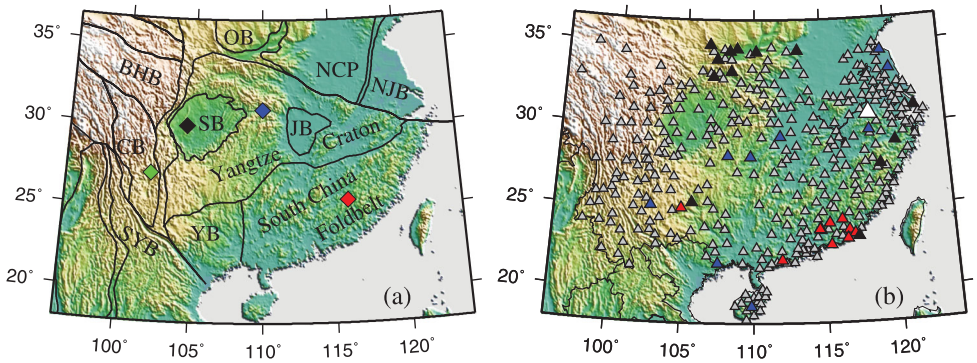

Figure 1. (a) Tectonic map of South China. Thick lines indicate the boundaries of the major tectonic units and basins, after Zhang *et al.* (1984) and Zhang *et al.* (2003). The South China Block comprises the Yangtze Craton, which encompasses the Sichuan Basin (**SB**) and the Jianghan Basin (**JB**), the South China Foldbelt, and the Youjian Block (**YB**). Other identified tectonic features are: **OB**, Ordos Basin; **NCP**, North China Platform; **NJB**, North Jiangsu Basin; **BHB**, Bayan Har Block; **CB**, Chuandian Block; **SYB**, South Yunnan Block; **YB**, Youjiang Block. The four colored diamonds identify locations referred to in Figs 12 and 13 (CB: green; SB: black; Yangtze craton, blue; South China Foldbelt, red). (b) The 387 CEArray stations for which we have instrument response files are shown with variously colored triangles; the 354 used in this study are shown in grey or white. The large white triangle is the location of station AHJIX referred to in Fig. 6. The blue, red, and black triangles identify the problematic stations where the problem is mislocation, π phase error, or an unknown (perhaps time variable) problem with the instrument response, respectively.

in South China extending from periods of 6–70 s based on ambient noise and earthquake tomography and construction of a 3-D Vsv model of the crust and uppermost mantle to a depth of 150 km. Ambient noise has been shown to be strong across China (e.g. Yang & Ritzwoller 2008b) and ambient noise tomography is performed from 6 to 40 s period. Earthquake tomography is performed from 25 to 70 s period across the study region. In the period band of overlap (25–40 s), we average the phase velocity maps from ambient noise and earthquakes, weighting up the ambient noise maps at the short period end and earthquake maps at the long period end. The eikonal tomography method (Lin *et al.* 2009) is used to produce the Rayleigh wave phase speed maps using both ambient noise and earthquake data. Eikonal tomography is a ray theoretic method but it models rays bent by lateral variations in structure and produces meaningful uncertainty estimates in the resulting dispersion maps. For the ambient noise, we demonstrate consistency for the phase velocity maps derived using eikonal tomography and the straight ray tomography method of Barmin *et al.* (2001). We also produce group velocity maps based on the method of Barmin *et al.* In addition, we demonstrate consistency between the phase velocity maps produced from ambient noise and earthquakes in the period band of their overlap.

Because a large number of disparate agencies in China are responsible for operating and maintaining the provincial seismic networks that compose CEArray, to combine data from all of these networks across the region of study requires careful quality control. The procedures that we have developed to insure the quality of the phase (i.e. traveltime) response of the vertical component of the CEArray stations are described in Section 2.1. After discarding 71 of the original 425 stations, we find that the resulting data set is of very high quality. The fraction of stations with problems on the vertical component (∼9 per cent) is much lower than that uncovered by an analysis of horizontal components of a larger set of CEArray stations by Niu & Li (2011) who found that about one-third of the stations have some sort of problem, including misorientation of the two horizontal components, mislabelling and polarity reversals in one or more of the components.

The goal of this study and related papers of Zheng *et al.* (2010b, 2011) and Yang *et al.* (2010, 2011) is to make significant strides toward developing an integrated, highly resolved shear wave speed (Vs) model of the crust and uppermost mantle beneath all of China. Zheng *et al.* (2011) focus on northeast China and Yang *et al.* (2010, 2011) on Tibet. The complementary focus of this paper is southeast China and this paper also applies earthquake data to extend the dispersion maps to longer periods. The purpose of this paper is to establish the quality of the surface wave data in South China, present the broad-band dispersion maps that result from ambient noise and earthquake data, demonstrate their consistency and robustness, and present a preliminary 3-D Vsv model of the crust and uppermost mantle. The resolution of structures that emerges in South China is unprecedented.

2 DATA AND METHODS

2.1 Data quality control

The primary means to assess and control the quality of the data is by measuring the consistency between the Rayleigh wave phase traveltimes observed between different stations using ambient noise. The measurement of Rayleigh wave group and phase traveltimes between stations is described in Section 2.2. Consistency is determined from the ability of smooth phase speed maps (such as those shown later in Fig. 9) to fit the measured traveltimes. For each station at a given period, we compute the difference between the observed traveltime to every other station and the traveltime to that station predicted by the phase velocity map at that period. This is an iterative process; as stations are discarded the phase velocity maps are updated and the process reinitiates.

An example at 20 s period is shown for a station judged to be acceptable (CQSHZ) in Fig. 2. The histogram in Fig. 2(a) is quite narrow, though there are a few outliers that turn out to be caused by other problematic stations (not CQSHZ). Traveltime residuals (observed minus predicted) between CQSHZ and other stations are plotted in Fig. 2(b) at each of the other station locations, identifying the locations of the large misfits with darker coloured reds or blues. The standard deviation of misfit for good central stations is typically less than or equal to 2 s. The average misfit relative to this station is about −0.2 s, meaning that the observed traveltimes are on average less than the predicted traveltimes, or the observed

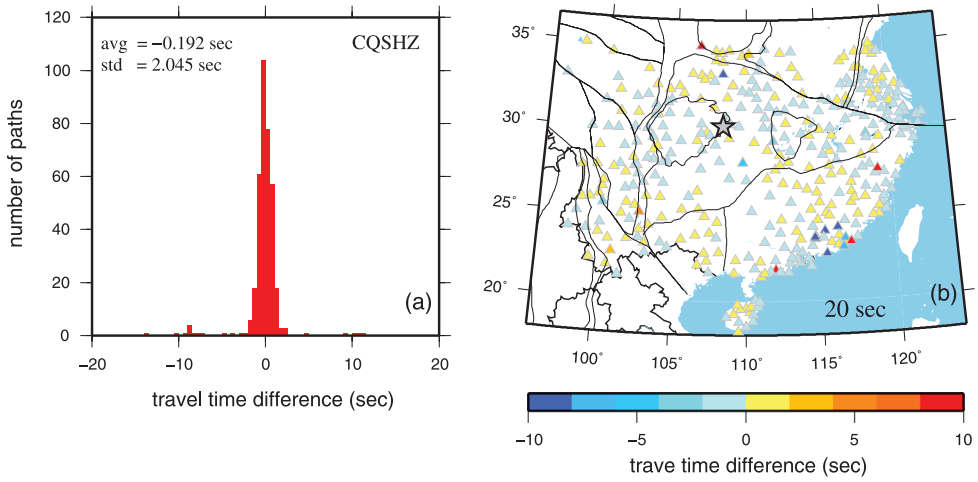

Figure 2. (a) Example of the misfit histogram for a station (CQSHZ) that is determined to be of good quality. The histogram presents the difference between the interstation Rayleigh wave phase travel time at 20 s period observed with ambient noise and the travel time at the same period predicted by the phase velocity map determined in this study (Fig. 9c). The average and standard deviation of the misfit are listed. (b) The location of station CQSHZ is shown with a large star and differences between the observed and predicted traveltimes between this and all other stations are colour coded. Positive values (red colours) indicate that the observed time is longer than that predicted (velocity is slower).

waves are slightly faster than predicted. However, if the average is taken using only measurements within one standard deviation of the mean, the average misfit is of much smaller amplitude, −0.05 s, implying that the overall average is perturbed from zero largely by other stations with instrumental problems.

The result shown in Fig. 2 is for a station that is retained for further analysis. There are more problematic stations, however, and several examples at 20 s period are shown in Fig. 3. Figs 3(a) and (b) illustrate a station (HNJIS) that is mislocated by about 1.5 km. This is revealed by the dipolar misfit pattern observed in Fig. 3(b). Using this method, nine stations are determined to be mislocated, and these stations are identified in Fig. 1(b) with blue triangles. In principle, we could relocate these stations using the misfit data, but we simply discard them because they are few in number and not concentrated in one area. An unknown, perhaps time variable, instrument response error is revealed in Figs 3(c) and (d) for station SNLOXT. There are 13 of these stations that are identified in Fig. 1(b) with black triangles. These stations are also discarded even though several are clustered in Shaanxi province, because we do not know how to correct them. A better understood π (10 s) instrument response problem is illustrated in Figs 3(e) and (f), which is diagnostic of a polarity error. The bi-modal misfit pattern seen in Fig. 3(e) scales with period. However, this problem also does not seem to be rectifiable. When we correct the apparent polarity error the resulting waveforms still disagree with waveforms observed at nearby stations, implying that the π-misfit reflects a more profound error. Thus, we also discard the 11 stations in this category that are identified in Fig. 1(b) with red triangles, most of which reside in Guangdong Province. The resulting list of 33 problematic stations is presented in Table 1. We also do not have instrument response files for 38 additional stations.

Removal of the 33 problematic stations and the 38 stations for which we lack response files results in a set of 354 stations for which we possess response files that are determined to be of good quality. These are the stations that are used for both ambient noise and earthquake tomography in southeast China. Based on these stations alone, Fig. 4 presents the phase traveltime misfits at periods of 8, 14, 20, and 30 s from ambient noise, again comparing the observed interstation traveltimes to those predicted from dispersion maps such as those plotted in Fig. 9. Rayleigh wave phase traveltime misfits average about 1 s below 30 s period, which is a quality statistic consistent with results using USArray (e.g. Lin *et al.* 2008). As Fig. 5 shows, group traveltime misfits are higher because group velocity is a more difficult measurement than phase velocity. A factor of 3 ratio between the misfit for group and phase times is commonly observed.

Although the effect of the Kyushu microseismic signal (e.g. Zheng *et al.* 2011) caused by Aso volcano can be seen in some cross-correlations across the northeastern part of the study region, the degradation of the cross-correlations and dispersion measurements obtained from them is minimal. Thus, it was not necessary for us to follow the more stringent data quality control measures advocated by Zheng *et al.* (2011).

2.2 Ambient noise data processing

The use of ambient noise to extract surface wave empirical Green's functions (EGFs) and to infer Rayleigh wave (e.g. Sabra *et al.* 2005; Shapiro *et al.* 2005) group and phase speeds in continental areas is well established (e.g., Bensen *et al.* 2007; Moschetti *et al.* 2007; Lin *et al.* 2008). The resolution of ambient noise tomography is limited primarily by the number, distribution and quality of stations. Southeast China possesses a large number of well-distributed stations that, after quality control procedures have been applied, yields a data set of very high quality. It is, therefore, an ideal location for ambient noise tomography. We process 2 years of continuous vertical component ambient noise observed at 354 seismic stations in South China. Thus, the cross-correlations contain predominantly Rayleigh waves.

The data processing procedures we adopt here follow those of Bensen *et al.* (2007) and Lin *et al.* (2008). Continuous data are decimated to one sample per sec and are then filtered in the period band from 5 to 50 s. Instrument responses are then removed from the continuous data because different types of seismic sensors are used; most are BB (long period corner at 20 s) but some are VBB (120 s corner) or UBB (360 s corner). Accurate surface wave dispersion measurements can be obtained at periods well above the

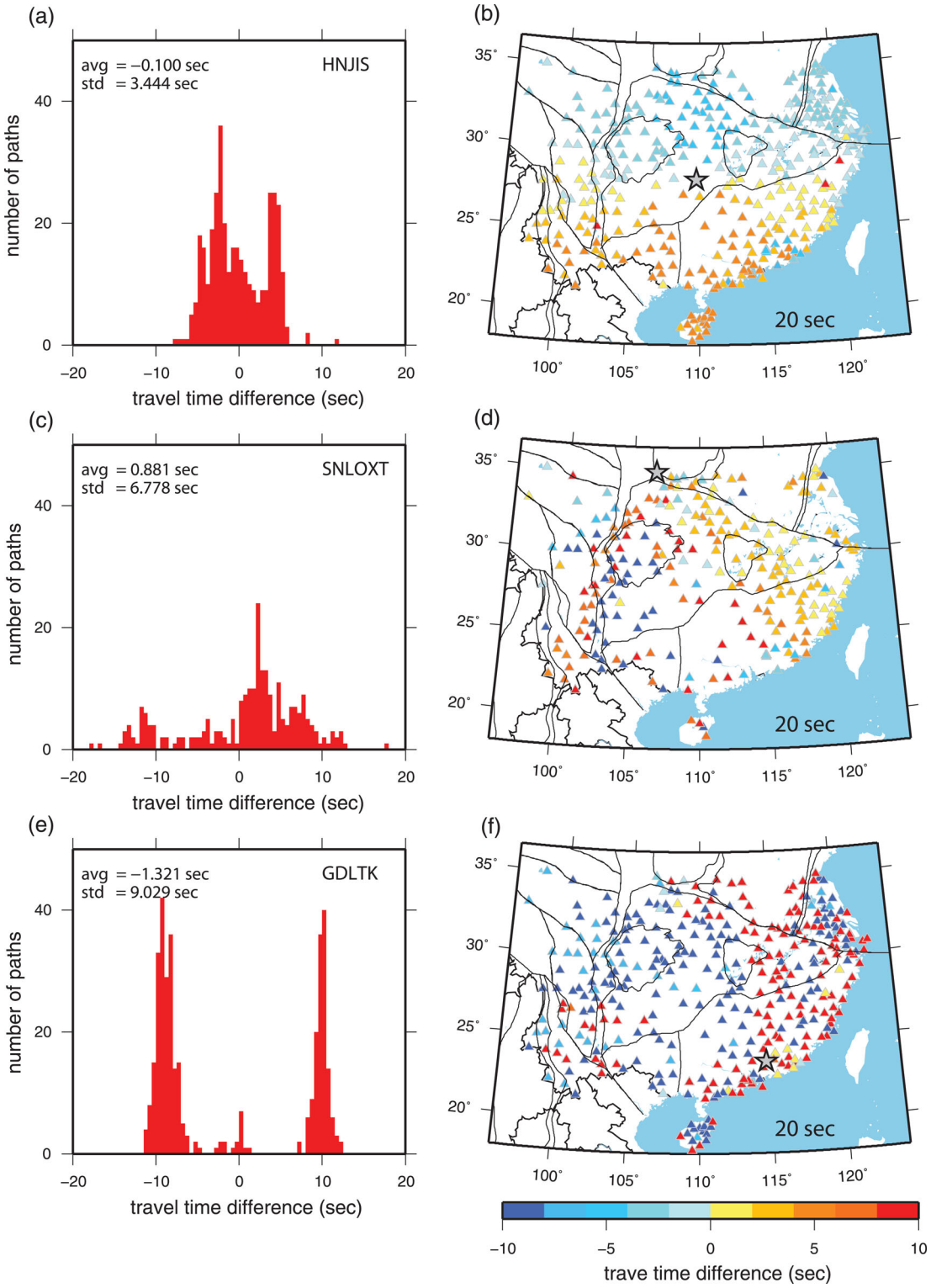

Figure 3. Examples of problematic stations. (a) and (b) Similar to Fig. 2, but for station HNJIS which is believed to have a location error of about 1.5 km. (c) & (d) Similar to (a) & (b), but for station SNLOXT which has an unknown, perhaps time-variable, problem with the instrument response. (e) & (f) Also similar to (a) & (b), but for station GDLTK which is believed to have a π phase error.

corner period of the instrument. Time-domain normalization in a running window 80 s in length is applied to suppress the influence of earthquake signals and other irregularities and spectral whitening is applied to flatten spectra over the entire period band (5–50 s). After completing these processing steps, cross-correlations are performed daily between pairs of stations in the period band from 5 to 50 s and then are stacked over the two-year time window.

Fig. 6 displays an example cross-correlation record section between Chinese station AHJIX and other stations in South China. Strong surface wave signals are observed on both positive and

Table 1. Problematic stations.

Problem with vertical component	Station name	If identified as problematic by Niu & Li (2011)
Mislocated	AHHUA, GXGXS, GZDJT, HNJGS, JSXIY,JSYC	No
	HIQZN, HNJIS, YNKMI	Yes
Instrument response error 1 (perhaps time variable)	GDNAP,HAJS, SNHUYT, SNHZHT, SNNSHT, SNTABT, SNQLIT, SNJYAT, ZJQIY, ZJYOK	No
	GZZFT, SHNAH, SNLOXT	Yes
Instrument response error 2 (π error)	GDCHZ,GDHYJ, GDLCH, GDMEZ, GDSHW, GDXIG, GDYGJ, GZXYT	No
	GDLTK, GDNAO, GDTIX	Yes

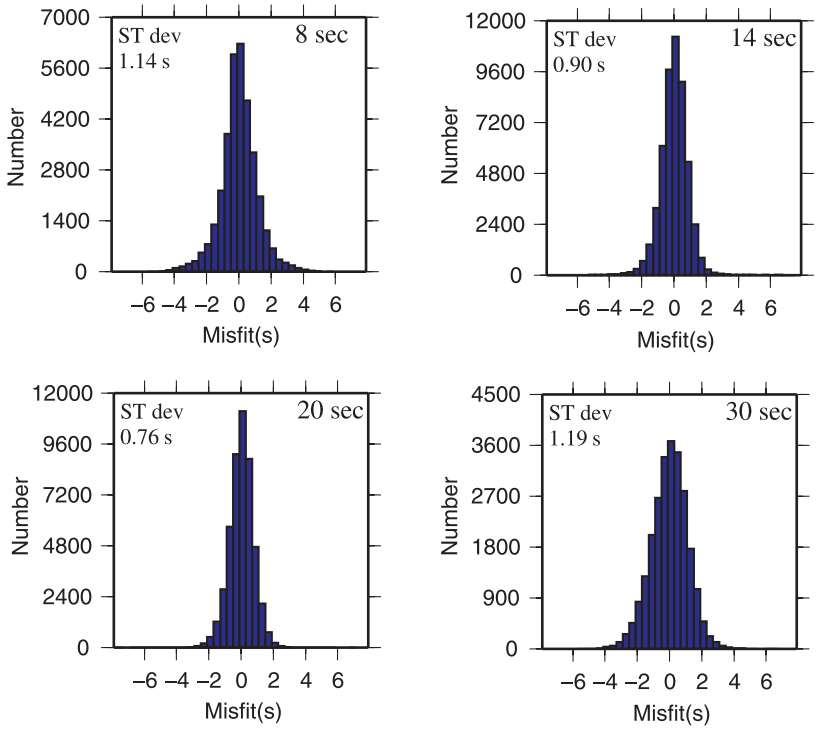

Figure 4. Histograms of Rayleigh wave phase travel time misfit between the travel times measured from the ambient noise cross-correlations using data that pass quality control procedures and travel times predicted from the phase velocity maps at each period. The standard deviation of the distribution is listed on each panel.

negative correlation lags. To simplify data analysis and enhance the signal-to-noise ratio (SNR) of the surface waves, we separate each cross-correlation into positive and negative lag components and then add the two components to form the so-called 'symmetric component'.

Group and phase velocity dispersion measurements of Rayleigh waves are obtained from the symmetric components of interstation cross-correlations by automatic frequency-time analysis (FTAN; Bensen *et al.* 2007). Group velocity is measured on the envelope of the surface wave packet and phase velocity measurements are made on the phase content of the wave packet. Group and phase velocity are not constrained to agree even though they are related theoretically (e.g. Levshin *et al.* 1999). The automated FTAN dispersion measurements are winnowed by applying three criteria to select reliable measurements for surface wave tomography. (1) The distance between two stations must be greater than three wavelengths for group velocity and two wavelengths for phase velocity to ensure sufficient separation of the surface wave packets from precursory noise. (2) SNR must be greater than 15 at each period for the measurement at that period to be accepted. (3) As described in Section 2.1, we require that the measurements agree with one another across the data set. Measurements that can be fit well by a smoothed tomographic map are considered to cohere within the data set as a whole. Based on this analysis, 33 stations are rejected, as discussed in Section 2.1, yielding 354 stations judged to have acceptable response files. In addition, at each period we discard all measurements that are misfit by the phase velocity map at that period by more than half a period. This effectively removes 2π phase errors. Resulting misfit statistics are listed in Table 2.

In principle, 354 stations could produce up to about 62 000 cross-correlations. The smaller numbers presented in Table 2, ranging up to about ∼50 000 paths between 12 and 20 s period,

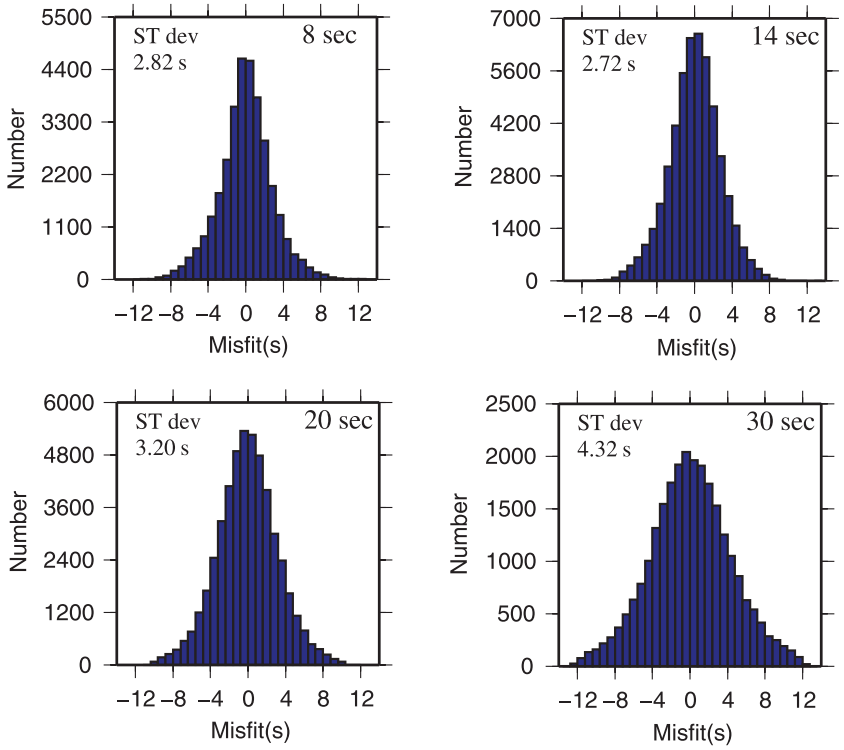

Figure 5. Same as Fig. 4, but for group velocity.

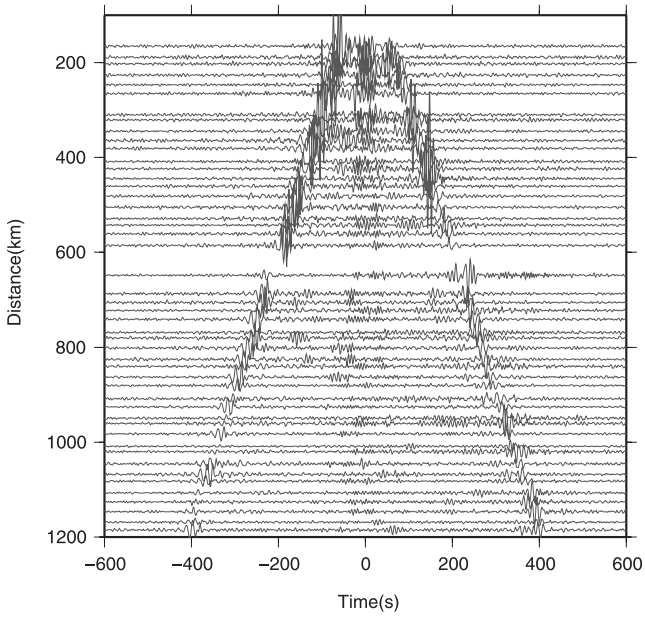

Figure 6. Two-year cross-correlations filtered between periods of 5 and 50 s are shown between seismic station AHJIX (white triangle in Fig. 1b) and other stations. Rayleigh waves appear at both negative and positive correlation lag times with a move-out of about 3 km s^{-1}. Arrivals near zero time are probably mostly teleseismic body waves, which are not studied here.

principally reflects the strength of ambient noise in China, which reduces above ∼25 s period. Still, even at 40 s period more than 12 000 paths remain. Also, at periods below ∼10 s, scattering from small-scale heterogeneities makes measurement of surface wave speeds more difficult. Phase velocity measurements generally out-

Table 2. Final number of measurements and misfit as a function of period for ambient noise.

Period (s)	Numbers		Misfit (s)	
	Group	Phase	Group	Phase
6.00	19120	20726	2.37	1.03
8.00	32066	34546	2.82	1.14
10.00	41017	45369	2.86	1.15
12.00	46666	50356	2.86	1.02
14.00	49336	52191	2.72	0.90
16.00	49951	52171	2.76	0.79
18.00	49967	51141	3.15	0.74
20.00	47767	48907	3.20	0.76
25.00	36427	38159	3.89	0.88
30.00	24911	27066	4.32	1.19
35.00	16841	18570	4.79	1.32
40.00	10981	12630	4.90	1.51

number group velocity measurements because of differences in the interstation distance data selection criterion.

We perform surface wave tomography on the selected dispersion measurements to produce Rayleigh wave group and phase velocity maps on a 0.5° × 0.5° grid using the straight ray tomography method of Barmin *et al.* (2001) as well as eikonal tomography, which models ray bending due to lateral heterogeneities (Lin *et al.* 2009). A comparison between the results of these two methods is presented in Fig. 7 for the 20 s Rayleigh wave phase velocity determined from ambient noise. The results are quite similar; in particular, the mean across each map differs only by 0.2 m s^{-1}. The similarity of the maps produced by these two methods results because the relatively short paths considered here are not strongly affected by off-great circle effects at this period (e.g. Lin *et al.* 2009). At shorter periods (e.g. 10 s) near the Sichuan Basin, differences are somewhat stronger, however. Because eikonal tomography produces uncertainty

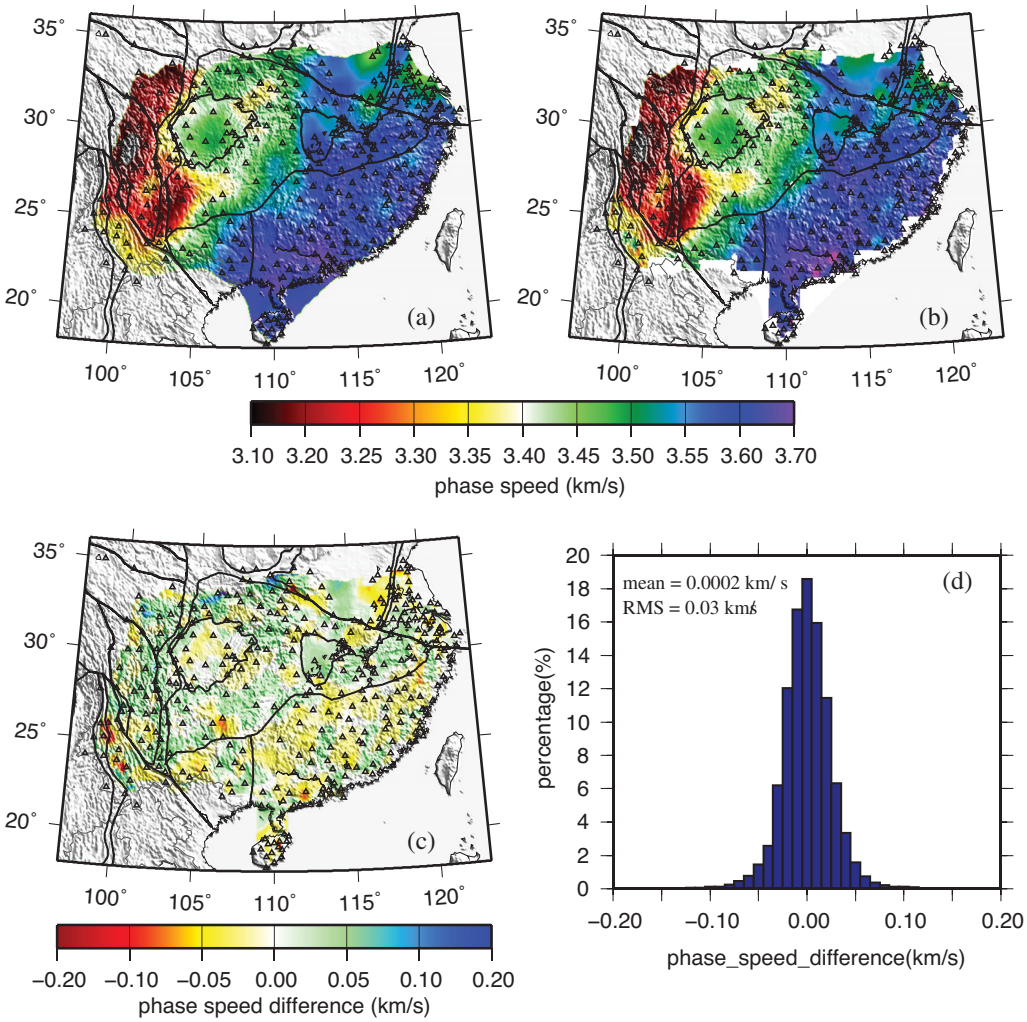

Figure 7. Comparison of the 20 s Rayleigh wave phase velocity maps constructed with (a) straight ray tomography (Barmin *et al.* 2001) and (b) eikonal tomography (Lin *et al.* 2009) using ambient noise. (c) Map of the difference between the results in (a) and (b). (d) Histogram of the differences between results in (a) and (b).

estimates for the maps, we present the results here using that method for phase velocities (Fig. 9). However, the eikonal equation governs propagation of phase not group times; thus, for group velocities we use the straight ray tomography method of Barmin *et al.* (2001) with confidence given the similarity of the methods evidenced in Fig. 7. We ignore finite frequency effects here, because they are weak in the period band in which ambient noise is applied here (e.g. Lin & Ritzwoller 2011; Ritzwoller *et al.* 2011).

Rayleigh wave group velocity maps from ambient noise data are presented in Fig. 8 at periods of 8, 14, 20, and 30 s. Similarly, the phase velocity maps from ambient noise are presented in Figs 9(a)–(c) and 10(a). We examine the maps in subsequent sections, after discussing earthquake data processing, which is applied at periods greater than 25 s.

Misfit statistics for the final tomographic maps provide information about the quality of the dispersion measurements. Below 30 s period, in the primary passband of Chinese BB instruments, phase traveltime misfit is about 1 s and group traveltime misfit is several times larger, the typical relationship between phase and group traveltime misfits. Misfit degrades below 10 s due to scattering from small-scale heterogeneities that makes group and phase velocity measurements more difficult and also because it is more difficult to resolve 2π phase ambiguities. Misfit also increases above 30 s period because of reduction in the level of ambient noise, long period roll-off of many of the instruments, and because paths are typically longer at longer periods, on average. Overall, misfit statistics establish that data quality is high, particularly between 10 and 30 s period where misfits are similar to those derived from USArray data in the US (e.g. Lin *et al.* 2008).

2.3 Earthquake data processing

We apply the eikonal tomography method described by Lin *et al.* (2009) to earthquake data to determine Rayleigh wave phase speed maps from 25 to 70 s period. Earthquake waveforms are accumulated following all events with surface wave magnitudes greater than 5.0 that occurred in the years 2009 and 2010. This yielded a set of 595 earthquakes within 15 000 km from the centre of the array. Phase traveltimes are tracked across the array following each earthquake for all stations where SNR is greater than 10 at a given period and the 2π phase ambiguity is resolved. Unless SNR $>$ 10 at a given period for $>$50 stations, the earthquake is discarded for that period. This results in about 500 earthquakes at 25 s period and diminishes to about 300 earthquakes at 70 s period. Finite frequency

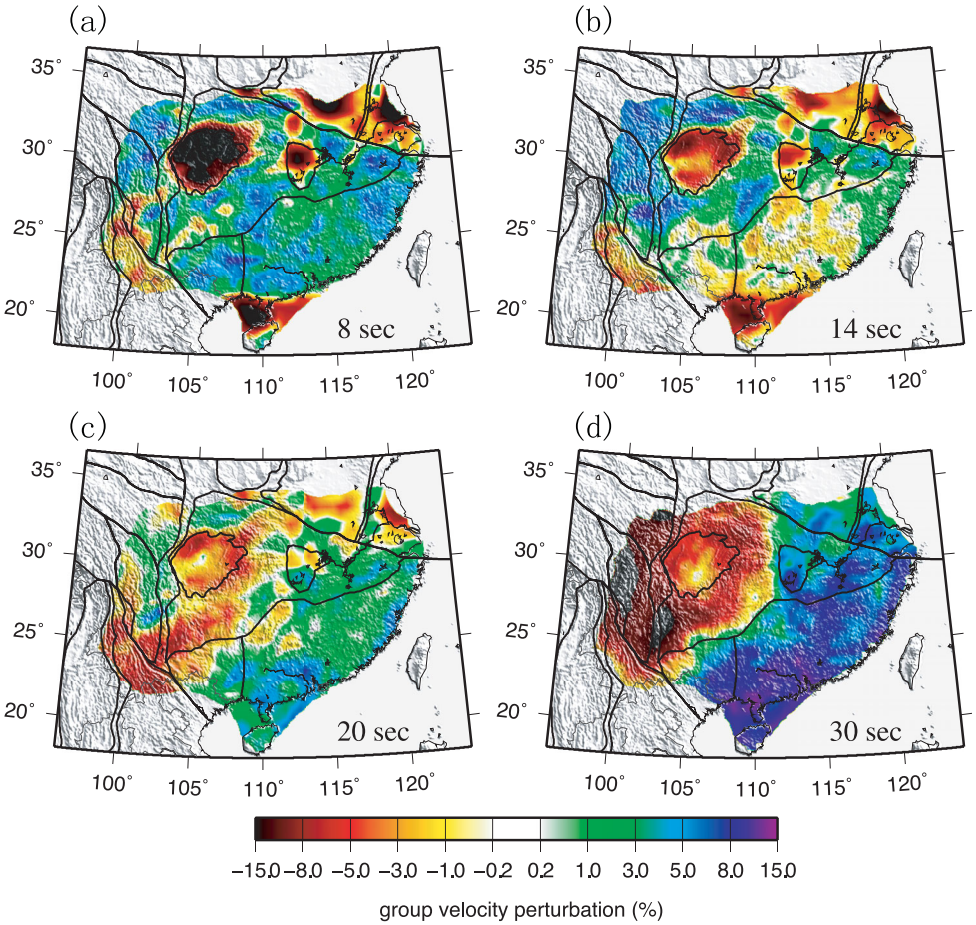

Figure 8. Rayleigh wave group velocity maps at periods of (a) 8, (b) 14, (c) 20 and (d) 30 s determined from ambient noise using the straight ray method of Barmin *et al.* (2001). Maps truncate (revert to grey shades) where resolution is worse than 100 km. Average group velocities at these periods are 2.9488, 2.9177, 2.9514 and 3.2937 km s^{-1}, respectively.

effects are ignored in the eikonal tomography method, though ray bending due to lateral structural variations is modelled. We have obtained maps to periods >70 s, but to use them finite frequency effects should be modelled (Lin & Ritzwoller 2011). One approach would be to apply the Helmholtz tomography method of Lin & Ritzwoller (2011), but this method utilizes amplitude information and the amplitude responses of Chinese instruments are poorly known.

The earthquake based Rayleigh wave phase velocity map at 32 s period is compared with the map derived from ambient noise in Fig. 10. Generally, there is good agreement. The lateral variation of the difference between ambient noise and earthquake maps (Fig. 10d) is similar to differences between ray theories (Fig. 7d). The earthquake-derived map is faster by an average of about 12 m s^{-1} (0.3 per cent), however, but much of this difference is near the edge of the map. The agreement in the distribution and amplitude of the anomalies is typical for comparisons between ambient noise and earthquake-derived maps (e.g. Yang & Ritzwoller 2008a; Ritzwoller *et al.* 2011), and the disparity in the mean of the maps is also similar to what is observed using USArray in North America (Yang & Ritzwoller 2008a).

3 DISPERSION MAPS

Rayleigh wave group and phase velocity maps are produced on a 2-s-period grid from 6 to 20 s period and then on a 5-s-period grid to 70 s period. Ambient noise maps extend up to 40 s period and earthquake derived maps from 25 to 70 s period. In the period band of overlap of the methods (25–40 s), the two measurements are averaged locally as are the uncertainties. The ambient noise measurement is given more weight at the short period end and the earthquake measurement is weighted up at longer periods. What emerges is a phase velocity dispersion curve with uncertainties from 6 to 70 s period. The group velocity curve is derived only from ambient noise and extends only from 6 to 40 s period. Group velocity uncertainty at each location and period is taken as twice the phase velocity uncertainty. Uncertainties are discussed further two paragraphs below.

Examples of these maps from ambient noise at 8, 14, 20 and either 30 or 32 s period are shown in Figs 8, 9(a)–(c), 10(a). Velocity perturbations are plotted only where resolution is better than 100 km, where resolution is defined as twice the standard deviation of a 2-D Gaussian fit to the resolution surface at each geographic node (Barmin *et al.* 2001). At each period, the group velocity anomalies are sensitive to shallower structures than the phase velocities. Thus, for example, phase velocity maps should be compared with shorter period group velocity maps. (Sensitivity kernels are presented by Zheng *et al.* (2011) and in many other papers, so we do not present them here.) Earthquake-derived phase velocity maps at 32, 40, 50, and 70 s period are shown in Figs 9(d)–(f) and 10(b).

The method of eikonal tomography provides uncertainties in the dispersion maps. Examples at periods of 20 and 40 s are presented in Fig. 11, where the shorter period result is from ambient noise

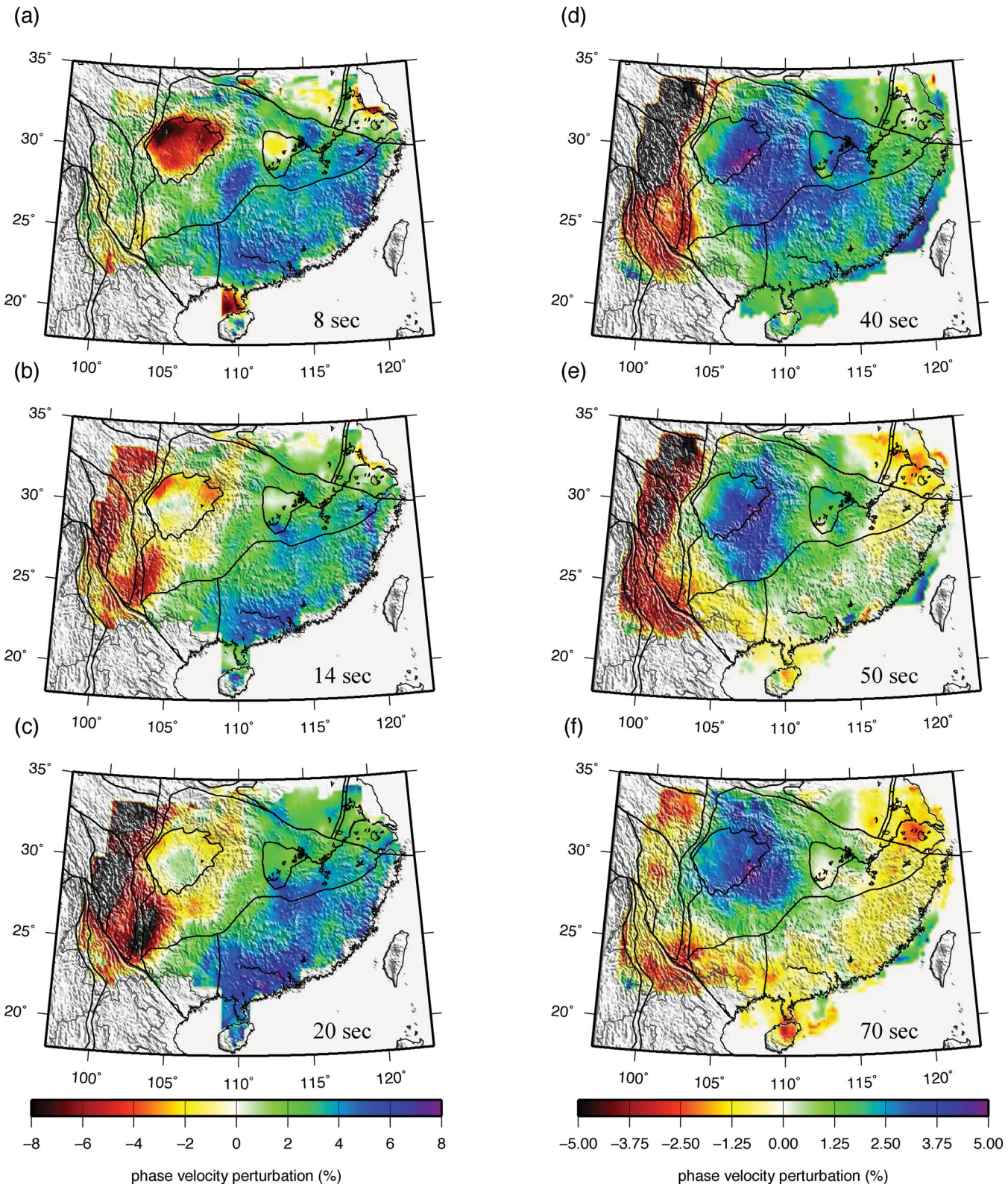

Figure 9. Rayleigh wave phase velocity maps constructed by eikonal tomography applied to ambient noise data at periods of (a) 8, (b) 14, and (c) 20 s. Average phase velocities at these periods are 3.1261, 3.2747 and 3.4708 km s^{-1}, respectively. Similar maps constructed from earthquake data based on eikonal tomography are shown for (d) 40 s, (e) 50 s and (f) 70 s period, where average phase velocities are 3.8427, 3.9081 and 3.9823 km s^{-1}, respectively. As in Fig. 8, maps truncate where resolution is worse than 100 km.

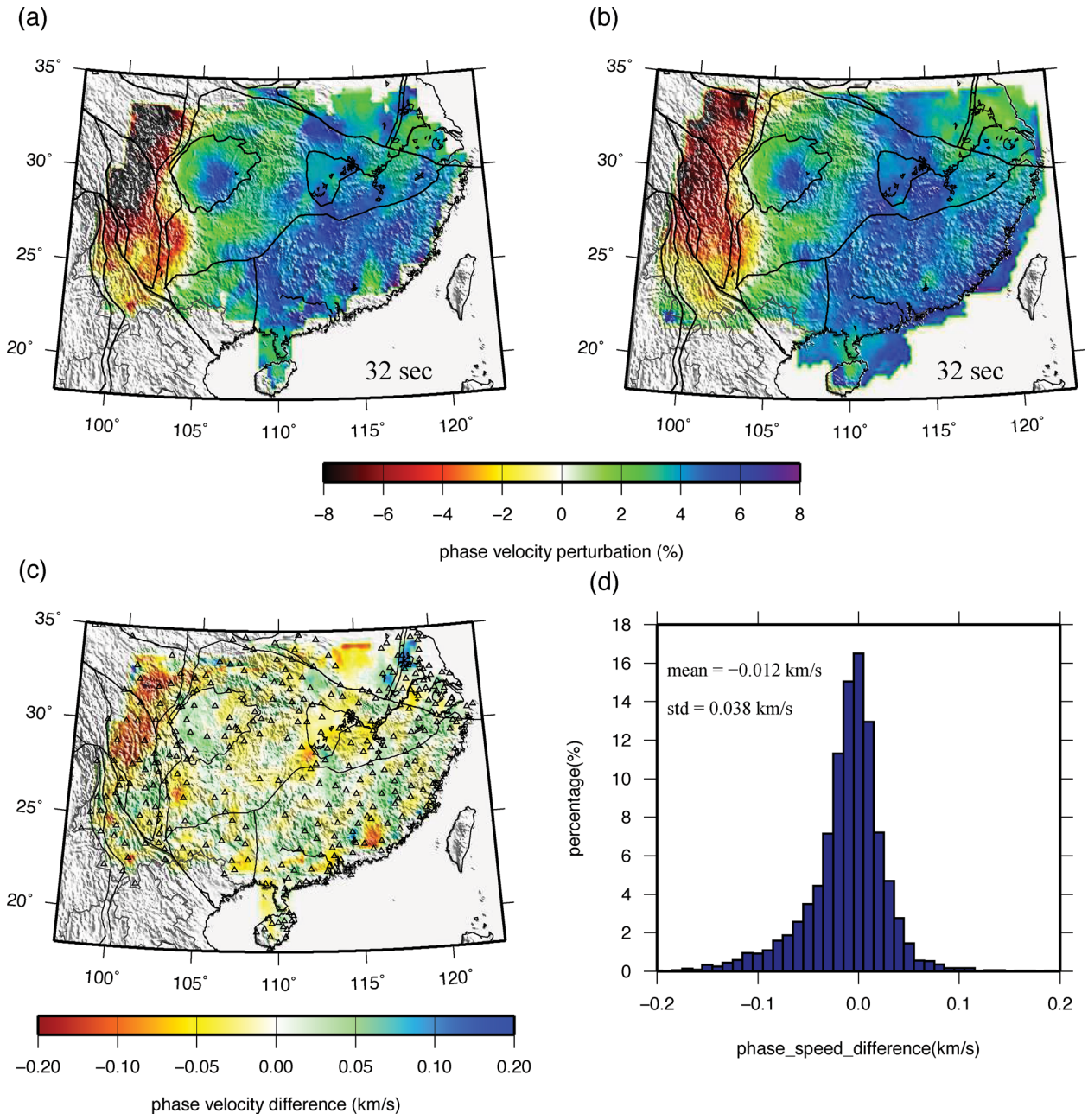

Figure 10. (a) Ambient noise derived phase velocity map at 32 s period (avg = 3.7479 km s^{-1}). (b) Earthquake derived phase velocity map at 32 s period (avg = 3.7609 km s^{-1}). (c) Difference between the maps shown in (a) and (b). (d) Histogram of the differences presented in (c).

and the longer period result derives from earthquakes. Except near map boundaries, the uncertainties are largely spatially invariant. The average uncertainty at 20 s is 10 m s^{-1} and at 40 s is 18 m s^{-1}, and uncertainties typically grow near the edges of the maps. Uncertainties determined from ambient noise by eikonal tomography are generally underestimated (e.g. Lin *et al.* 2009). The reason for this underestimation is not entirely understood, but is believed to result from the fact that the ambient noise measurements between a target station and different nearby stations are not entirely independent. When we compute the local standard deviation of the measurements to estimate local uncertainty, we divide by the square root of the number of interstation measurements at that point. If the measurements are not entirely independent, however, we should divide by a smaller but unknown number. We find that doubling the uncertainty of measurements obtained from ambient noise brings them into better agreement with the uncertainties from earthquakes. We also ensure that uncertainties are not less than 10 m s^{-1} at any period or location. Realistic uncertainties result, similar to those presented for ambient noise across the western US by Lin *et al.* (2009).

The short period maps, e.g. 8 and 14 s group velocity and 8 s phase velocity, are strongly influenced by the shallow part of the crust, particularly the existence of sediments. The major sedimentary basins, such as the Sichuan Basin, Jianghan Basin, the North China Plain, North Jiangsu Basin and the South China Sea between the mainland and Hainan Island, all appear as low velocities. The boundary between the South China Block and the North China Platform is clear because of sediments deposited near the boundary of these regions. The 14 s group velocity map (Fig. 8b) also shows a

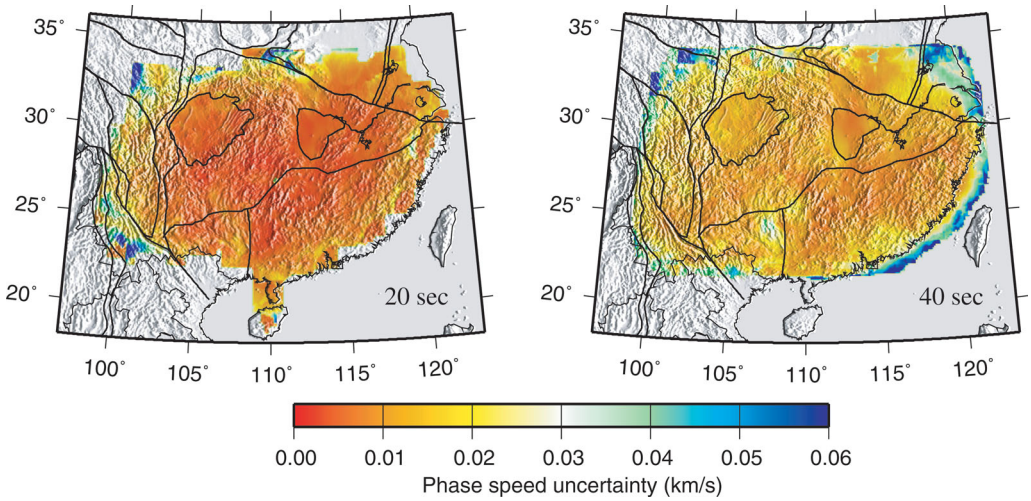

Figure 11. Examples of raw uncertainties estimated for the Rayleigh wave phase velocity maps by eikonal tomography for (left) ambient noise at 20 s period (avg = $\sim$10 m s^{-1}) and (right) earthquake data at 40 s period (avg = $\sim$18 m s^{-1}).

clear distinction between the South China Foldbelt and the generally faster Yangtze Craton. At short periods, the Youjian Block is not distinguishable from the South China Fold Belt.

At intermediate periods, 20–32 s, the maps are affected by mid- to lower-crustal shear wave speeds and crustal thickness. At these periods, the velocity features lose the geological coherence seen at shorter periods; the predominant structure is a west-to-east velocity variation. For example, the 30 s group velocity and the 20 s phase velocity maps are quite similar. The Yangtze Craton is roughly bifurcated on these maps, being slow in the west and fast in the east, reflecting thicker crust in the west (Zhang *et al.* 1984; Teng *et al.* 2003). At these periods, the Youjian Block is distinguishable from the South China Foldbelt, perhaps because of the influence of active tectonics driven by the expansion of Tibet in the western part of the study region. However, the eastern Yangtze Craton and South China Foldbelt are not distinguishable, consistent with the expectations or results of earlier studies (Li & Mooney 1998; Huang *et al.* 2003).

The deepest sensitivity of these maps is provided by the longest period maps (e.g. 40–70 s phase velocity maps in Figs 9d–f). The 32 s phase velocity maps (Fig. 10) remain strongly sensitive to crustal thickness where thicker crust appears as lower velocities. The 40 s map also is sensitive to crustal thickness, but reflects upper mantle shear wave speeds more strongly. This difference in sensitivity accounts for differences between the 32 and 40 s phase velocity maps. Very low phase velocities are imaged for the Bayan Har, Chuandian, and South Yunnan Blocks. This is expected for these actively deforming regions with thicker crust. A prominent high velocity anomaly appears on the 50–70 s maps in the western Yangtze Craton reflective of high wave speeds in the upper mantle and thick mantle lithosphere. This and other features of the resulting model are discussed further in Section 5.

4 CONSTRUCTION OF THE 3-D VSV MODEL

This study is based exclusively on Rayleigh waves, which are sensitive to vertically polarized shear wave speeds (Vsv) that may be slower than horizontally polarized shear speeds (Vsh) in regions where anisotropic minerals are preferentially aligned in the horizontal plane. The velocity difference between Vsv and Vsh is referred to as radial anisotropy. Thus, the model we produce is a Vsv model. In the presence of substantial radial anisotropy, Vsv can be several percent lower than the effective isotropic shear wave speed, Vs. Radial anisotropy is common in both the mantle (e.g. Ekstrom & Dziewonski 1998; Shapiro & Ritzwoller 2002) and the crust (e.g. Shapiro *et al.* 2004; Moschetti *et al.* 2010a,b), and is geographically variable. We will generally refer to our 3-D model as being a Vsv model, but for simplicity will also refer to it as shear wave speed or Vs model.

The 3-D Vsv model is estimated using the Rayleigh wave phase velocity maps from 6 to 70 s period and group velocity maps from 6 to 40 s period with attendant uncertainties on a 0.5° × 0.5° grid across the study region. Local dispersion curves from the four locations identified with diamonds in Fig. 1(a) are shown in Fig. 12 with error bars. The error bars are period dependent and for Rayleigh wave phase velocity represent one standard deviation uncertainties determined by eikonal tomography at each period, as discussed in Section 3. Group velocity maps are not determined with eikonal tomography, thus they result entirely from ambient noise (not earthquakes) using the method of Barmin *et al.* (2001) up through 40 s period.

As discussed in the previous section, the ambient noise and earthquake-derived maps are merged in the period band of overlap of the methods, between periods of 25 and 40 s. The ambient noise and earthquake-derived maps are weighted up at the short and long period ends of this range, respectively. The ambient noise and earthquake-derived uncertainties result from the same weighting scheme applied to the individual dispersion maps. The group velocity uncertainty is twice the phase velocity uncertainty at each period.

The 3-D model is constructed via a Monte–Carlo method that is similar to the methods of Shapiro & Ritzwoller (2002) and Yang *et al.* (2008) but is more closely related to the method of Shen *et al.* (2011). We summarize the method briefly here.

Starting from the global Vsv model of Shapiro & Ritzwoller (2002), uniformly distributed perturbations in Vsv are considered using a single sedimentary layer with variable thickness and shear velocity, four B-splines for Vsv in the crystalline crust, and five B-splines in the mantle to a depth of 200 km, below which the model is a constant velocity half-space. The resulting model is vertically smooth in both the crystalline crust and mantle. Moho

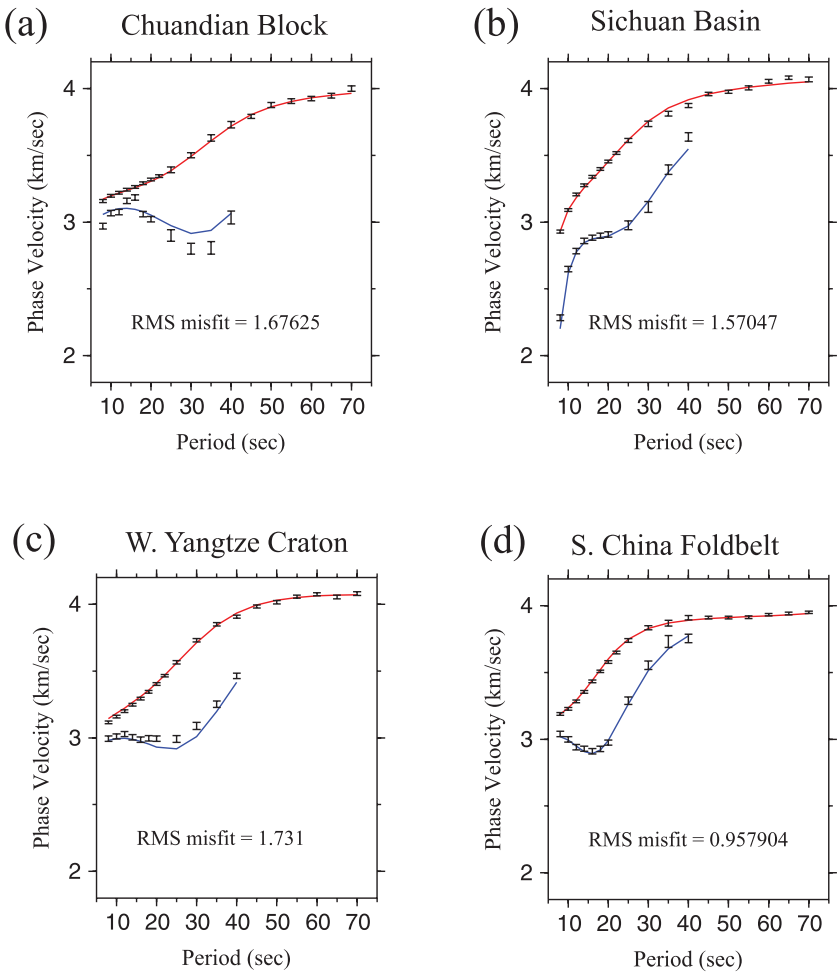

Figure 12. Dispersion curves at different locations: Chuandian Block, Sichuan Basin, Yangtze Craton, and South China Foldbelt. Locations are indicated by the green, black, blue, and red diamonds in Fig. 1(a), respectively. Rayleigh wave phase (red lines) and group (blue lines) velocities predicted from the best fitting Vs model are compared with the measured values (error bars) extracted from the dispersion maps at each location. Square-root of reduced χ^2 misfit is listed as 'RMS misfit'.

depth is allowed to vary in a uniform interval of ± 10 km relative to the starting model. Vsv is constrained to increase monotonically in the crust and the depth derivative of velocity directly below Moho is constrained to be positive (i.e. velocity increases with depth right below Moho, but can decrease deeper into the mantle). Both constraints are introduced to reduce the volume of model space searched and have the effect of reducing the magnitude of the trade-off between Moho depth and structures at depths adjacent to Moho.

The application of the crustal monotonicity constraint and the constraint on the positivity of the uppermost mantle velocity gradient requires more discussion. The crustal monotonicity constraint is the less problematic of the two. Except in Tibet, we find that we can fit the data well without crustal low velocity zones in the region of study. Thus, we have no data-driven reason to allow a crustal low velocity zone in South China east of Tibet. That does not mean that low velocity zones do not exist locally, only that we have no evidence for their existence outside of Tibet. In contrast, Yang *et al.* (2012) see clear evidence for crustal low velocity zones in eastern Tibet and the crustal monotonicity constraint is not invoked in that study. In our view, allowing low velocity zones in South China would needlessly increase estimates of uncertainty in the middle crust. The justification for the positivity constraint on the uppermost mantle velocity gradient is not as strong. It has been invoked because surface waves alone cannot resolve the gradient and its application reduces trade-offs in the inversion near Moho. The inability of surface waves to resolve the velocity gradient in the uppermost mantle is one of the strongest reasons to assimilate receiver functions in the inversion (e.g. Shen *et al.* 2011).

The model has no radial anisotropy, thus Vs = Vsh = Vsv. Also, we assume that the crystalline crust is a Poisson solid and set Vp = 1.73 Vs, in the sediments we use Vp = 2.0 Vs, and for density we use the scaling relation advocated by Christensen & Mooney (1995): $\rho = 0.541 + 0.3601$ Vp, where ρ is in g cm^{-3} and Vp is in km s^{-1}. We apply a physical dispersion correction (Kanamori & Anderson 1977) using the Q-model from PREM (Dziewonski & Anderson 1981), and the resulting model is reduced to 1 s period.

Models are chosen randomly guided by a Metropolis algorithm (e.g. Mosegaard & Tarantola 1995) and are judged to be acceptable if the reduced χ^2 misfit to the dispersion curves is less than 0.5 units greater than the minimum misfit, $\chi^2_{\min}$ at each location. Reduced χ^2 misfit is defined as follows:

$$\chi^2 = \frac{1}{N}\sum_{i=1}^{N}\frac{(d_i - p_i)^2}{\sigma_i^2}$$

where N is the total number of discrete dispersion measurements along the phase and group velocity curves, d_i is one of the measurements with uncertainty σ_i, and p_i is the predicted dispersion measurement (Rayleigh wave phase or group speed) for the considered model. RMS misfit (square root of reduced χ^2) averages about 1.3 across the region of study, establishing both the plausibility of the uncertainty values and the ability of the dispersion curves to be fit by a vertically smooth Vsv model with the imposed constraints. Much of the misfit results from phase velocities above 40 s period and group velocities from 20 to 40 s period. Uncertainties in both appear to be slightly underestimated, but not at a level to affect the final model appreciably.

As examples, the procedure yields the four ensembles of models presented in Fig. 13 for the four pairs of dispersion curves shown in Fig. 12. The ensemble is represented by the grey shaded region, which presents two standard deviations around the mean at each depth in each direction. The dispersion curves predicted by the best-fitting model are shown in Fig. 12 as the blue (group velocity) and red (phase velocity) lines. The RMS misfit listed on each of the panels of Fig. 12 is the square root of the reduced χ^2 value. The Vsv model that we show here and its uncertainty are defined by the middle and quarter-width (1σ) of the ensemble at each depth, respectively. The uncertainties in the model are largest where shear wave speeds trade-off effectively with boundary topography, which occurs near free boundaries in the model: Moho and the base of the sedimentary layer. This is why uncertainties grow near the top of the crystalline crust and both above and below Moho.

Fig. 14 shows the Vsv model at two depths in both the crust (10 km, 25 km) and the mantle (70 km, 140 km). Because the dispersion curves only extend to 70 s period, the model is not reliable beyond a depth of ∼150 km. Crustal thickness and uncertainty are shown in Fig. 15 and uncertainties at the depths shown in Fig. 14 are presented in Fig. 16. Four vertical slices of the model are presented in Fig. 17 on profiles along 30°N latitude, 110°E longitude, a diagonal profile extending from the northwest to southeast part of the study region, and 115°E longitude, identified with lines in Fig. 14 (lower right panel). The model is discussed further in Section 5.

Model uncertainties are shown in Fig. 16 corresponding to the depth slices in Fig. 14. At each depth, uncertainties tend to be bifurcated, being relatively constant and low over an extended region, but growing larger elsewhere. This bifurcation is caused by the elevation of uncertainties due to the trade-off between perturbations in shear velocity near a boundary and topography on that boundary. The closeness to a boundary changes over the region at each depth. For example, the trade-off between Vs at 10 km depth (Fig. 16a) with sediment thickness only occurs in sedimentary basins where sediments are thickest, namely in the northern Sichuan Basin. Uncertainties at 10 km depth exceed 150 m s^{-1} (>5 per cent) below the Sichuan Basin whereas across most of South China they are less than 50 m s^{-1} (∼1.5 per cent). At 25 km depth (Fig. 16b), uncertainties are small where this depth is most distant from the Moho, which occurs where the crust is thickest, namely in the western part of the study region where uncertainties average about 50 m s^{-1} (∼1.3 per cent). However, in the eastern Yangtze Craton and South China Foldbelt, uncertainties are about twice as large on average (>3 per cent). This is because 25 km depth is in the lower crust in these regions, relatively close to the Moho, and is in the middle crust in the western part of the study region. Uncertainties in Moho depth (Fig. 15) are more uniform than the velocities but are somewhat larger in the western than the northern and eastern parts of the study region. Thus, uncertainty in Moho depth is larger where crust is thicker, averaging about 4 km in the western Yangtze Craton and about 3 km beneath the South China Foldbelt. At 70 km depth, uncertainty averages about 60 m s^{-1} across most of the study region, but grows to 2–3 times this value in Tibet. This is also a crustal thickness effect because the Moho is deep enough beneath Tibet to trade-off with seismic velocities at 70 km. Uncertainties are higher on average at 140 km, generally more than 100 m s^{-1}, due to weaker constraints on structure at this depth.

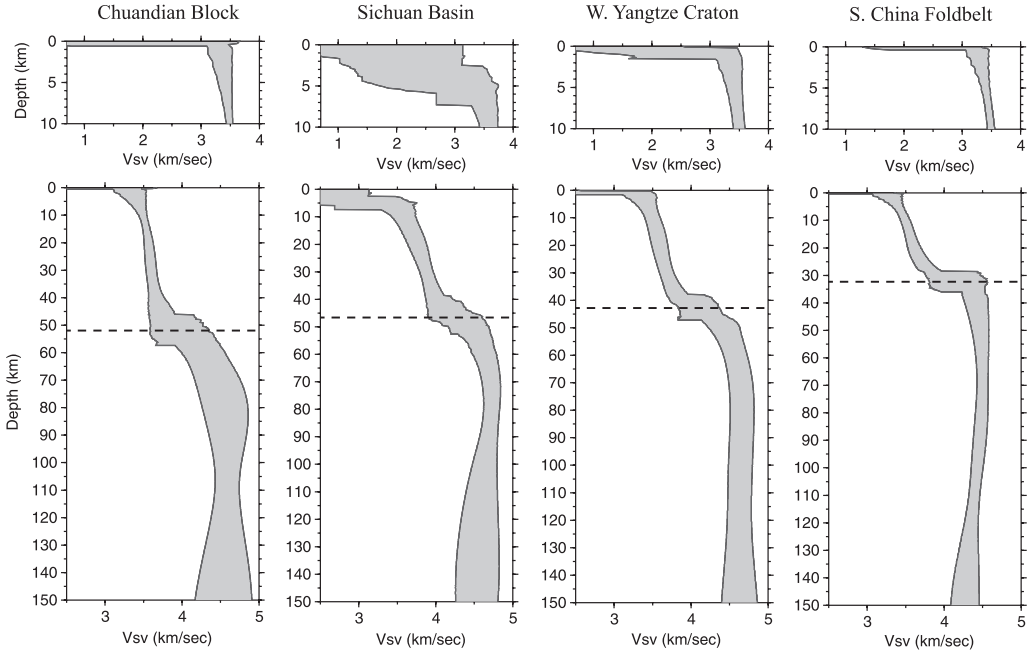

Figure 13. Ensemble of accepted models determined from each of the corresponding pairs of dispersion curves in Fig. 12. (Top Row) Shallow Vs structure: 2σ corridor of acceptable models between the surface and 25 km depth, highlighting the shallow crust. (Bottom Row) Full Vs model: 2σ corridor of acceptable models between the surface and 150 km depth, highlighting crustal thickness (dashed line).

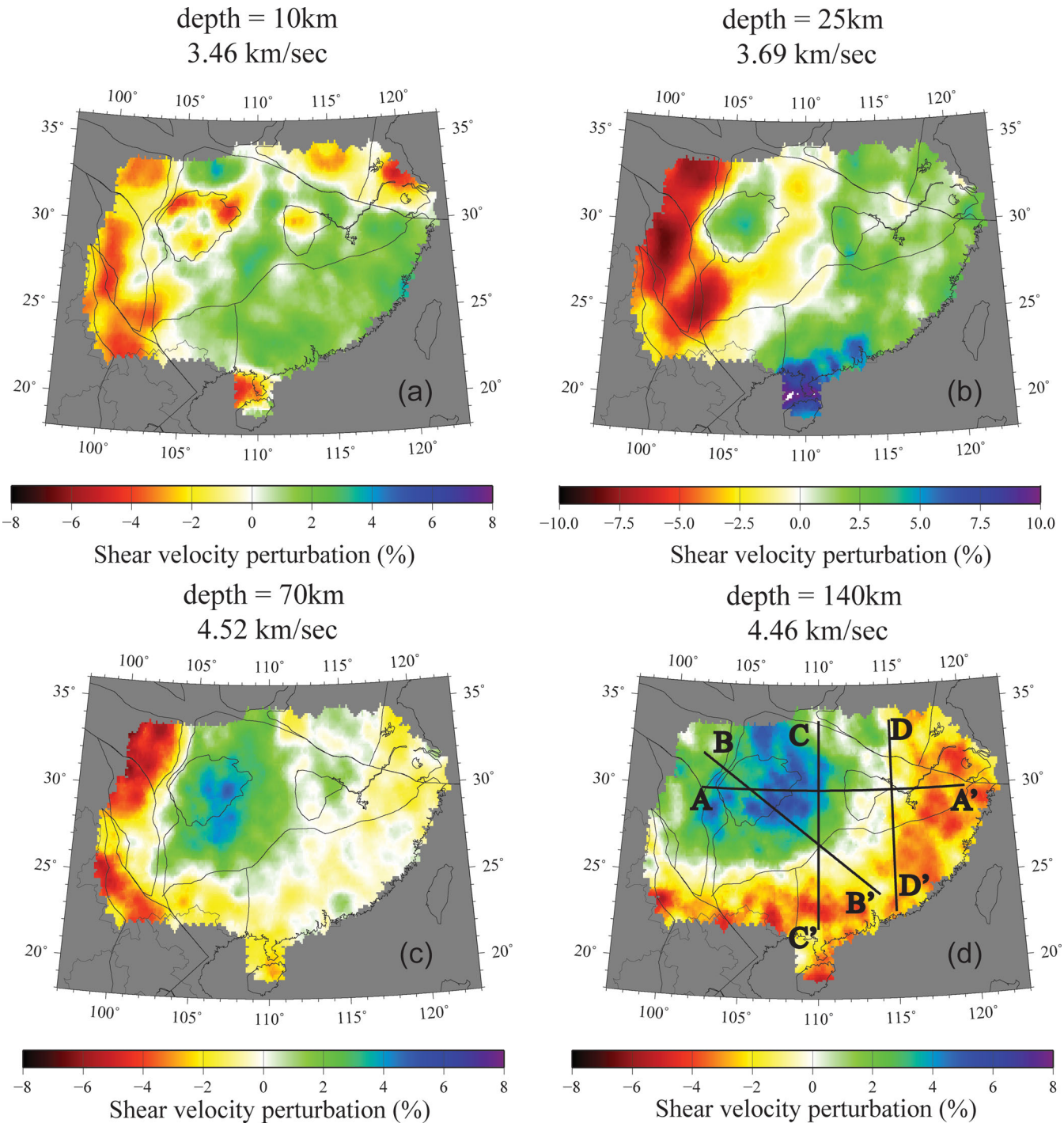

Figure 14. Horizontal slices of the estimated Vsv model (middle of the ensemble of accepted models at each depth) plotted at four depths (10 km, 25 km, 70 km and 140 km). Velocities are plotted as the percent deviation relative to the mean (shown) across the map at each depth. The straight lines in the lower right panel identify the locations of the vertical model slices shown in Fig. 17.

5 DISCUSSION

5.1 Structural features of the 3-D model

Shear velocities in the shallow crust at 10 km depth are fairly homogeneous across most of the study region being about 3.48 km s^{-1} across most of the eastern Yantgze craton and the South China Foldbelt. There are two primary exceptions. First, the principal velocity anomalies are the low wave speeds beneath the sedimentary basins, notably the Sichuan Basin, the Jianghan Basin, and offshore between Hainan Island and the mainland. The Sichuan and Jianghan basins may be seen more clearly in the vertical slices in Fig. 17, profiles A–A′, B–B′. The lowest wave speeds are observed beneath the northern Sichuan Basin. As discussed in the preceding section, shear wave speeds at depths near internal boundaries are not well determined. Sedimentary basins, in particular, do not have an entirely well defined lower boundary. Thus, exceptionally low velocities at 10 km depth beneath the basins may be caused by leakage from

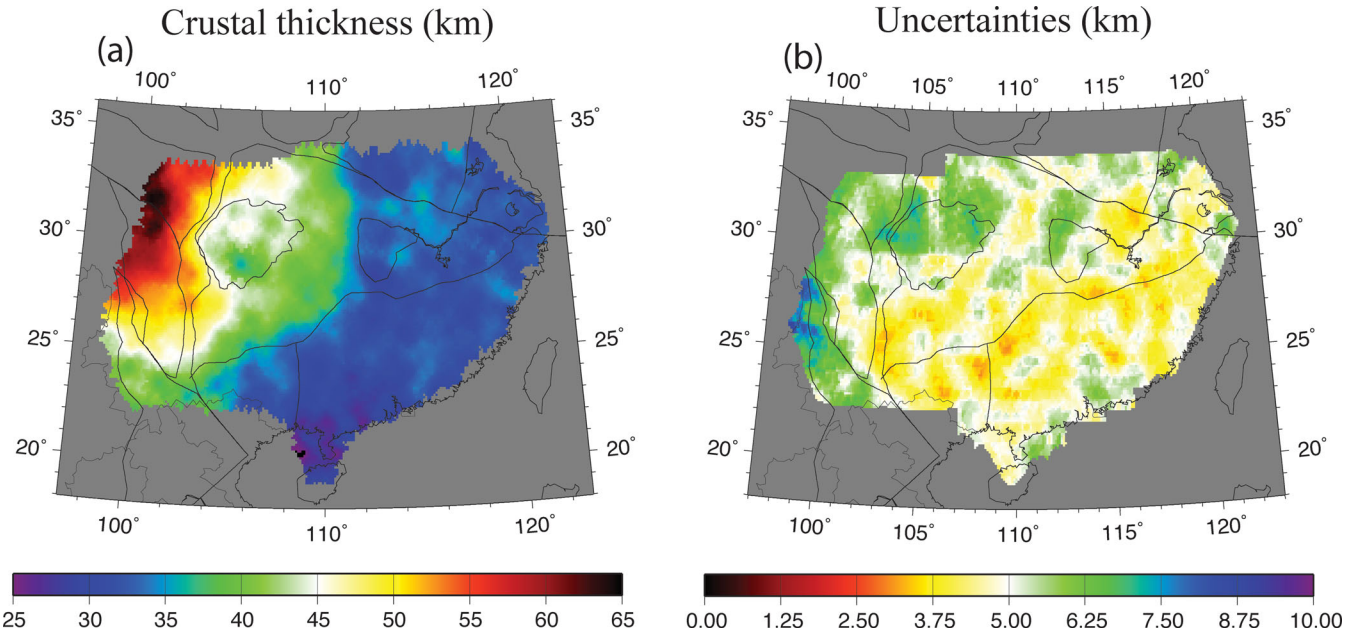

Figure 15. (a) Crustal thickness estimated across the study region (in km). (b) One standard deviation uncertainties estimated for crustal thickness (in km).

sediments at shallower levels. Secondly, the Tibetan crust at 10 km depth is also slow relative to the regional average, with a value ($\sim$3.35 km s^{-1}) that is consistent with the observation at 15 km depth by Yang *et al.* (2012). These low velocities are probably caused by elevated upper crustal temperatures beneath Tibet. There is a third, more subtle, variation worthy of note: the eastern Yantgze Craton is slightly faster at 10 km depth (avg: $\sim$3.55 km s^{-1}) than the South China Foldbelt (avg: $\sim$3.48 km s^{-1}) which is seen more clearly on the 14 s group velocity map shown in Fig. 8(b). This is probably reflective of differences in composition and thermal history between these two regions.

The deeper crust beneath the Sichuan Basin is quite fast, however, as can been seen in Figs 14(b) and 17, profiles A–A′, B–B′. The middle and lower crust beneath the Sichuan and Jianghan basins, therefore, are probably cold and rheologically stiff.

Deeper crustal shear wave speeds (e.g. Fig. 14b), Moho depth (e.g. Fig. 15a), and uppermost mantle shear wave speeds (e.g. Figs 14c, d) are best considered together. Exclusive of Tibet, the region of study breaks into two major subdivisions.

(1) The western Yangtze Craton is characterized by thick seismic lithosphere (>100 km), a crust mostly thicker than 40 km, but a relatively slow middle and lower crust (Fig. 14b) south and east of the Sichuan Basin. This low velocity middle and lower crust extends in a semi-circle around the southern and eastern parts of the Sichuan Basin and is discussed further in Section 5.2 below. The thick lithosphere can be seen clearly as high shear wave speeds on Figs 14(c) and (d), which extend to the base of the vertical profiles A–A′, B–B′, C–C′ seen Fig. 17. For the purposes here, we define the thickness of the seismic lithosphere as the depth in the mantle where shear wave speed dips below 4.5 km s^{-1}. Essentially, the entire western Yangtze Craton is faster than 4.5 km s^{-1} at 70 km depth with wave speeds underlying the Sichuan Basin reaching as high as 4.75 $\pm$ 0.06 km s^{-1}. We refer to the region with thick crust and mantle lithosphere beneath the western Yangtze Craton as the 'West Yangtze Block'. High velocities beneath the centre of the West Yangtze Block extend at least to 150 km (Fig. 14d, 17). West of the Yangtze Craton beneath Tibet high velocities also extend beneath 100 km (Fig. 14d).

(2) In contrast with the West Yangtze Block, the eastern Yangtze Craton and South China Foldbelt have a much thinner seismic lithosphere (<70 km), a thin crust ($\sim$30 km, seen clearly on profile D–D′ in Fig. 17, and higher mid- to lower-crustal shear wave speeds. Indeed, the seismic structure of the eastern Yangtze Craton is quite similar to the South China Foldbelt. There are two somewhat subtle differences, however. First, as seen in profile D–D′ in Fig. 17, the seismic mantle lithosphere beneath the eastern Yangtze Craton is thicker, averaging at least 80 km thickness, whereas beneath the South China Foldbelt the seismic lithosphere extends only to about 60–70 km, on average. Secondly, the asthenosphere beneath the South China Foldbelt is much slower than beneath the eastern Yangtze Craton, as can be seen clearly in Fig. 17 by contrasting profiles A–A′ and C–C′ and by inspecting profile D–D′.

Only a small segment of Tibet is included in the study region, mostly encompassed by the Chuandian tectonic belt along the western margin of the Yangtze Craton. Not surprisingly, the crust is determined to be very slow and thick in this region (>60 km in parts). Overall the structure is similar to that observed by Yang *et al.* (2012) in a study dedicated to Tibet.

5.2 Structures consistent with flat slab subduction beneath South China

As discussed in Section 5.1, there are profound structural differences between the western part of the Yangtze Craton and both the eastern Yangtze Craton and the South China Foldbelt. This led us to refer to the 'West Yangtze Block', a region with thick crust and mantle lithosphere that is presumably colder and stronger than the other parts of South China. These other parts notably include the eastern Yantze Craton, which is structurally much more similar to the South China Foldbelt than to the western Yangtze Craton. Differences do exist between the South China Foldbelt and the eastern Yangtze Craton, but they are much more subtle. The lithosphere is thinner and asthenospheric shear wave speeds are somewhat lower

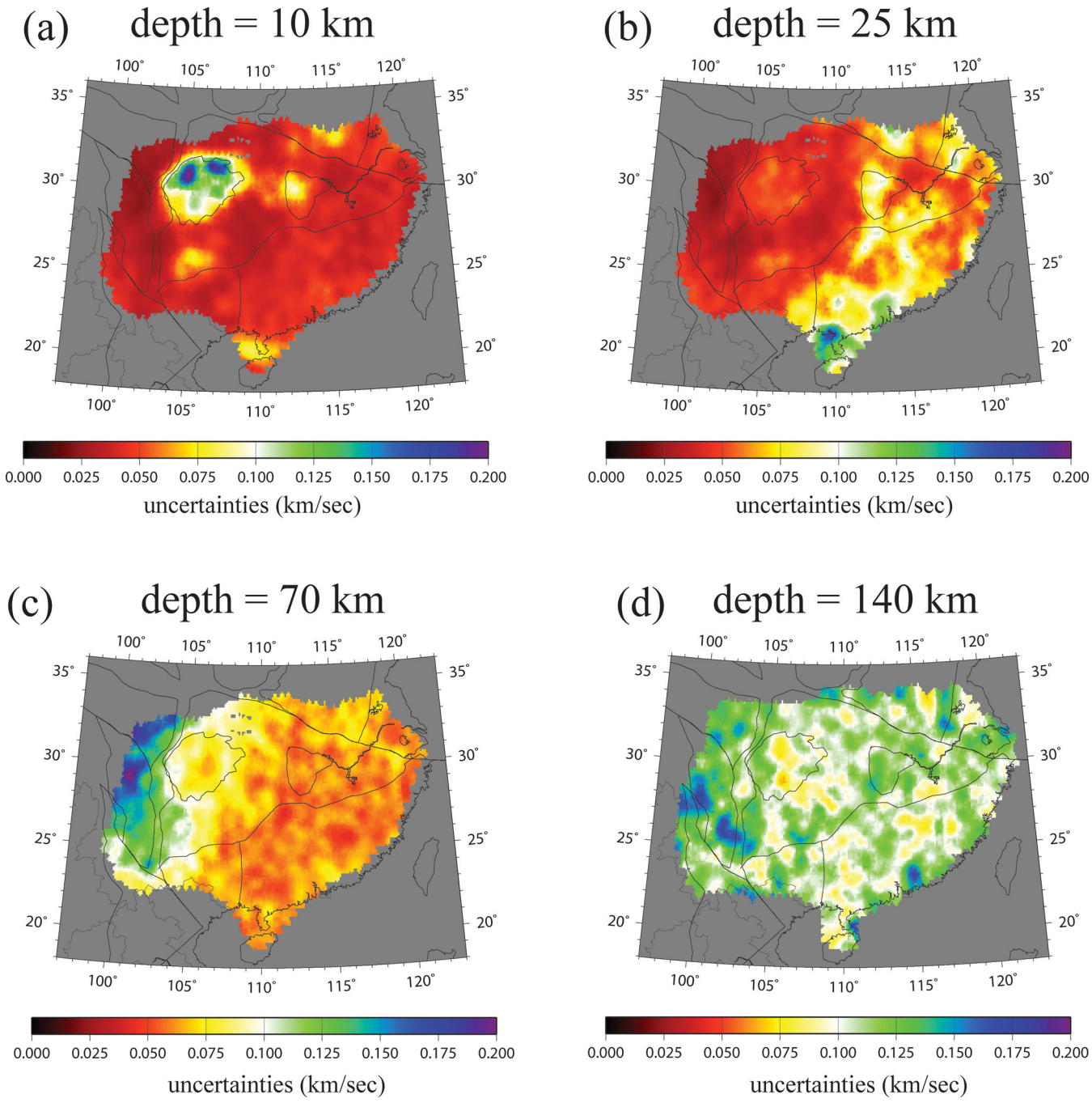

Figure 16. Model uncertainties (1 standard deviation) plotted at the same depths as the horizontal slices shown in Fig. 14.

in the South China Foldbelt than in the eastern Yangtze craton, which reflects a slightly weaker and perhaps warmer uppermost mantle beneath the South China Foldbelt.

The structural differences within South China reflect the geological evolution of the South China Block. Geochronologic studies reveal that the Yangtze Craton possesses prominent crustal components that date at least to the Neoproterozoic (e.g. Liu *et al.* 2008) and that it probably formed in the Archean (Gao *et al.* 1999; Qiu *et al.* 2000; Zhang *et al.* 2006a; Zheng *et al.* 2006). Archean rocks are also observed in the Kongling terrane of the Yangtze Gorges region (e.g. Zhang *et al.* 2006b). Since the Proterozoic, however, the Yangtze Craton has experienced two significant intercontinental collisions. First, the Cathaysia Block moved northward and merged with the Yangtze Craton during in late Precambrian at about 1.0–0.9 Ga (e.g. Shui 1988; Chen *et al.* 1991). The two blocks merged at about 0.9 Ga and have suffered little relative movement since. Secondly, the South China Block collided with the North China Block in the Permian to form the Qinling–Dabie suture zone (e.g. Enkin *et al.* 1992). The eastern part of the Qinling–Dabie belt is truncated by the Tancheng–Lujiang Fault (TLF), identified by the north–south striking double line in the northeast part of Fig. 1(a). The sinistral slip of the TLF is about 600 km, with material from the South China Block on the east side of the TLF moving northward in a long-term extensional process (e.g. Xu & Guang 1994). This extension may be a mechanism for the thinning of the crust and lithosphere in the North Jiangsu Basin east of the TLF, which is shown in Fig. 14(d).

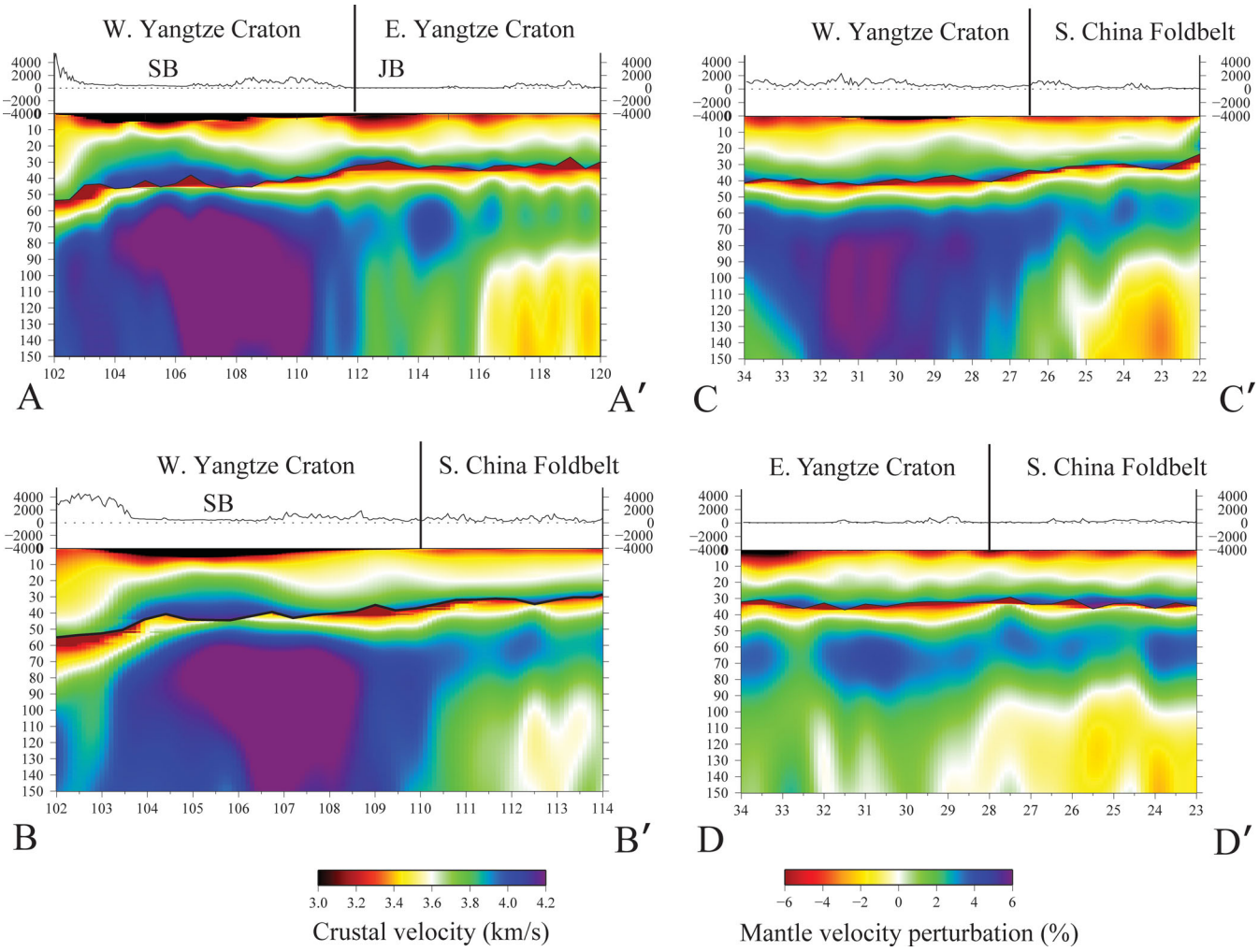

Figure 17. Vertical slices of the estimated Vs model (middle of the ensemble of acceptable models at each depth) plotted along the four profiles identified in the lower right panel of Fig. 14. Absolute velocities are presented in the crust and percent perturbations relative to 4.5 km s^{-1} are shown in the mantle. The thin black line is the Moho.

Neither of these collisions, however, explain the significant differences in crustal and lithospheric thickness between the western Yangtze Craton and the eastern Yangtze Craton. An important clue is provided by the existence of a 1300-km-wide intracontinental orogen that occurred during the Mesozoic (Li & Li 2007) between 250 and 195 Ma, progressing from the southeast coast of the South China Foldbelt to the eastern boundary of the Sichuan Basin (GSA data Repository item 2007041; Li & Li 2007). There is a nearly linear decrease of age from southeast to northwest with a gradient of about −0.7Ma km^{-1}, suggesting that this intracontinental orogen progressed slowly, with an average relative speed of about 1.8 mm a^{-1}.

Although a number of tectonic models have been designed to explain the evolution of this orogen (e.g. Hsu *et al.* 1990; Li 1998) as well as the resulting post-orogenic magmatism (e.g. Jahn *et al.* 1990; Gilder *et al.* 1996; Zhou & Li 2000), all suffer challenges to their acceptance (e.g. Chen *et al.* 1991; Gilder *et al.* 1991; Li *et al.* 2003; Wang *et al.* 2005). We believe that the flat slab subduction model proposed by Li & Li (2007) may illuminate the structural variations seen in our 3-D model. In their model, Li & Li propose that a flat slab subducted northwestward beneath South China and terminated at the boundary of the Sichuan Basin, creating a series of fold belts. During this process, heat generated by friction or small-scale convection in the uppermost mantle may have been responsible for lithospheric erosion and perhaps crustal thinning. This would be a plausible explanation for the eastward and southeastward thinning of the crust and lithosphere revealed by the 3-D model. Thus, in this interpretation, the West Yangtze Block is the residual of the Yangtze Craton that has not been eroded by Mesozoic flat slab subduction. Li & Li (2007) also hypothesize that upon termination of subduction, excess gravitational potential energy may have broken the middle part of the flat slab, causing rollback and generating post-orogenic magmatism. This additional reheating may explain why we observe a lower velocity asthenosphere beneath the South China Foldbelt than beneath the eastern Yangtze Craton, even though both regions suffered effects from flat slab subduction.

Flat slab subduction, however, probably does not explain the semi-circular low velocity feature that appears in the middle to lower crust (∼25 km) east and south of the Sichuan Basin in the western Yangtze Craton. Because the Sichuan Basin is rheologically strong and located at the eastern boundary of the active Tibetan Plateau, we speculate that these low crustal shear wave speeds result from the eastward movement of the Sichuan Basin relative to the Yangtze Craton, which can be observed by GPS measurements (Wang *et al.* 2001). Under this circumstance, the crust near the eastern boundary of the Sichuan Basin would have experienced compressive forces

and may have undergone deformation that has warmed the rocks of the lower and the middle crust and caused the semi-circular crustal low velocity belt.

6 CONCLUSIONS

The amalgamation of broad-band provincial seismic networks in China, which is referred to here as CEArray, presents a remarkable data resource. We apply quality control procedures to 2 years of continuous waveform data from CEArray to develop Rayleigh wave phase and group velocity maps from 6 to 40 s period with phase velocity maps extending up to 70 s period. Ambient noise and earthquake tomography are applied based on eikonal tomography to generate the phase velocity maps and a traditional ray theoretic procedure (Barmin *et al.* 2001) is applied to estimate the group velocity maps. A Monte–Carlo inversion method is used to estimate a 3-D Vsv model of the crust and uppermost mantle to a depth of 150 km beneath all of South China.

The principal observation is a clear image of the 'West Yangtze Block', a region of the western Yangtze Craton encompassing the Sichuan Basin with thick seismic lithosphere (>150 km), a crust mostly thicker than 40 km, but a relatively slow middle and lower crust in a semi-circular region south and east of the Sichuan Basin. The presumably cold and stable lithosphere of the West Yangtze Block contrasts with the eastern Yangtze Craton and South China Foldbelt that have a much thinner seismic lithosphere (<80 km), a thin crust (∼30 km) and higher mid- to lower-crustal shear wave speeds. The eastern Yangtze Craton and South China Foldbelt are structurally quite similar, but the South China Foldbelt has a thinner mantle lithosphere (60–70 km compared with ∼80 km) and better developed deeper asthenospheric layer.

This contrast in lithospheric structure between the West Yangtze Block and other parts of South China is consistent with and illuminated by the flat slab model of Mesozoic subduction proposed by Li & Li (2007). Flat slab subduction progressing northwestward beneath South China terminating at the boundary of the Sichuan Basin may have eroded the once much thicker mantle lithosphere of the eastern Yangtze Craton. The observed differences in the characteristics of the mantle lithosphere beneath the eastern Yangtze Craton and the South China Foldbelt may be traced to the formation of both regions prior to the Mesozoic or may reflect the post-orogenic magmatism that occurred beneath the South China Foldbelt that Li & Li hypothesize was caused by the breaking of the flat slab and subsequent slab rollback.

It is planned that future work will involve assimilation of receiver functions in the inversion to sharpen the image of the contrast between the crust and mantle and extension of data processing to include horizontal components in order to observe Love waves so that radial anisotropy in the crust and uppermost mantle can be inferred. Measurements of azimuthal anisotropy emerge naturally from the application of eikonal tomography, and inversion of these measurements to produce a model of azimuthal anisotropy in the crust and uppermost mantle also defines a natural follow-up to the research presented here.

ACKNOWLEDGMENTS

The authors thank two anonymous reviewers and Peter Molnar for helpful critical comments that have improved this paper. This work was performed while Drs. Longquan Zhou and Yong Zheng visited the University of Colorado for 1 year. The authors thank Dr. Fan-Chi Lin for help applying the eikonal tomography method. All waveform data used were obtained from the Data Management Centre of the China National Seismic Network at the Institute of Geophysics, China Earthquake Administration. This work was supported by US NSF-EAR award 0944022, US NSF-OISE subaward 0730154, the National Natural Science Foundation of China (41004036), and CAS grant kzcx2-yw-142.

REFERENCES

Barmin, M.P., Ritzwoller, M.H. & Levshin, A.L., 2001. A fast and reliable method for surface wave tomography, *Pure appl. Geophys.,* **158,** 1351–1375.

Bensen, G.D., Ritzwoller, M.H., Barmin, M.P., Levshin, A.L., Lin, F., Moschetti, M.P., Shapiro, N.M. & Yang, Y., 2007. Processing seismic ambient noise data to obtain reliable broad-band surface wave dispersion measurements, *Geophys. J. Int.,* **169,** 1239–1260.

Chen, J.F., Foland, K.A., Xing, F.M., Xu, X. & Zhou, T.X., 1991. Magmatism along the southeast margin of the Yangtze block: Precambrian collision of the Yangtze and Cathysia blocks of China, *Geology,* **19,** 815–818.

Christensen, N.I. & Mooney, W.D., 1995. Seismic velocity structure and composition of the continental crust: a global view, *J. geophys. Res.,* **100,** 9761–9788.

Dziewonski, A.M. & Anderson, D.L., 1981. Preliminary reference Earth model, *Phys. Earth planet. Int.,* **25**(4), 297–356.

Ekstrom, G. & Dziewonski, A.M., 1998. The unique anisotropy of the Pacific upper mantle, *Nature,* **394,** 168–172.

Enkin, R.J., Yang, Z.Y., Chen, Y. & Courtillot, V., 1992. Paleomagnetic constraints on the geodynamic history of the majot blocks of China from the Permian to the present, *J. geophys. Res.,* **97,** 13 953–13 989.

Gao, S., Ling, W.L., Qiu, Y., Zhou, L., Hartmann, G. & Simon, K., 1999. Contrasting geochemical and Sm-Nd isotopic compositions of Archean metasediments from the Kongling high-grade terrain of the Yangtze craton: evidence for cratonic evolution and redistribution of REE during crustal anatexis, *Geochem. cosmochim. Acta.,* **63,** 2071–2088.

Gilder, S.A., Keller, G.R., Luo, M. & Goodell, P.C., 1991. Timing and spatial distribution of rifting in China, *Tectonophysics,* **197,** 225–243.

Gilder, S.A. *et al*., 1996. Isotropic and paleomagnetic constraints on the Mesozoic tectonic evolution of south China, *J. geophys. Res.,* **101,** 16 137–16 154.

Hsu, K.J., Li, J., Chen, H., Wang, Q., Sun, S. & Sengör A.M.C., 1990. Tectonics of South China: key to understanding West Pacific geology, *Tectonophysics,* **183,** 9–39, doi:10.1016/0040-1951(90)90186-C.

Huang, Z.X., Su, W., Peng, Y.J., Zheng, Y.J. & Li, H.Y., 2003. Rayleigh wave tomography of China and adjacent regions, *J. geophys. Res.,* **108,** doi:10.1029/2001JB001696.

Jahn, B.M., Zhou, X.H. & Li, J.L., 1990. Formation and tectonic evolution of southeastern China and Taiwan: isotropic and geochemical constraints, *Tectonophysics,* **183,** 145–160.

Kanamori, H. & Anderson, D., 1977. Importance of physical dispersion in surface wave and free oscillation problems: review, *Revs. Geophys. Space Phys.,* **15**(1), 105–112.

Lebedev, S. & Nolet, G., 2003. Upper mantle beneath Southeast Asia from S velocity tomography, *J. geophys. Res.,* **108,** doi:10.1029/2000JB000073.

Levshin, A.L., Ritzwoller, M.H. & Resovsky, J.S., 1999. Source effects on surface wave group travel times and group velocity maps, *Phys. Earth planet. Int.,* **115,** 293–312.

Li, C. & van der Hilst, R.D., 2010. Structure of the upper mantle and transition zone beneath Southeast Asia from traveltime tomography, *J. geophys. Res.,* **115,** B07308, doi:1029/2009JB006882.

Li, S.L. & Mooney, W.D., 1998. Crustal structure of China from deep seismic sounding profiles, *Tectonophysics,* **288,** 105–113.

Li, X.H., Chen, Z., Liu, D.Y. & Li, W.X., 2003. Jurassic gabbro-granite syenite suites from southern Jiangxi province, SE China: age, origin, and tectonics significance, *Int. Geol. Rev.,* **45,** 898–921.

Li, Z.X., 1998. Tectonic history of the major East Asian lithospheric blocks since the mid-Proterozoic-A synthesis. *Am. Geophys. Un. Geodyn. Series,* **27,** 221–243.

Li, Z.X. & Li, X.H., 2007. Formation of the 1300-km-wide intracontinental orogen and postorogenic magmatic province in Mesozoic South China: a falt-slab subduction model, *Geology,* **35**(2), 179–182.

Lin, F.C., Moschetti, M.P. & Ritzwoller, M.H., 2008. Surface wave tomography of the western United States from ambient seismic noise: Rayleigh and Love wave phase velocity maps, *Geophys. J. Int.,* doi:10.1111/j1365-246X.2008.03720.x.

Lin, F.C., Ritzwoller, M.H. & Snieder, R., 2009. Eikonal Tomography: surface wave tomography by phase-front tracking across a regional broad-band seismic array, *Geophys. J. Int.,* **177**(3), 1091–1110.

Lin, F.C. & Ritzwoller, M.H., 2011. Helmholtz surface wave tomography for isotropic and azimuthally anisotropic structure, *Geophys. J. Int.,* **186,** 1104–1120.

Liu, X.M., Gao, S., Diwu, C. & Ling, W.L., 2008. Precambrian crustal growth of Yangtze craton as revealed by detrital zircon studies, *Am. J. Sci.,* **308,** 421–468.

Mosegaard, K. & Tarantola, A., 1995. Monte-Carlo sampling of solutions to inverse problems, *J. geophys. Res.,* **100**(B7), 12 431–12 447.

Moschetti, M.P., Ritzwoller, M.H. & Shapiro, N.M., 2007. Surface wave tomography of the western United States from ambient seismic noise: Rayleigh wave group velocity maps, *Geochem. Geophys. Geosys.,* **8,** Q08010, doi:10.1029/2007GC001655.

Moschetti, M.P., Ritzwoller, M.H. & Lin, F.C., 2010a. Seismic evidence for widespread crustal deformation caused by extension in the western USA, *Nature,* **464**(7290), 885–889.

Moschetti, M.P., Ritzwoller, M.H., Lin, F.C. & Yang, Y., 2010b. Crustal shear velocity structure of the western US inferred from amient noise and earthquake data, *J. geophys. Res.,* **115,** B10306, doi:10.1029/2010JB007448.

Niu, F. & Li, J., 2011. Component azimuths of the CEArray stations estimated from P-wave particle motion, *Earthq. Sci.,* **24,** 3–13.

Qiu, Y.M., Gao, S., McNaughton, N.J., Groves, D.I. & Ling, W.L., 2000. First evidence of 3.2 Ga continental crust in the Yangtze craton of south China and its implications for Archean crustal evolution and Phanerozoic tectonics, *Geology,* **28,** 11–14.

Ritzwoller, M.H. & Levshin, A.L., 1998. Eurasian surface wave tomography: group velocities, *J. geophys. Res.,* **103,** 4839–4878.

Ritzwoller, M.H., Levshin, A.L., Ratnikova, L.I. & Egorkin, A.A., 1998. Intermediate period group velocity maps across Central Asia, Western China, and parts of the Middle East, *Geophys. J. Int.,* **134,** 315–328.

Ritzwoller, M.H., Lin, F.C. & Shen, W., 2011. Ambient noise tomography with a large seismic array, *Compte Rendus Geoscience,* doi:10.1016/j.crte.2011.03.007.

Royden, L.H. *et al*., 1997. Surface deformation and lower crustal flow in eastern Tibet, *Science,* **276,** 788–790.

Sabra, K.G., Gerstoft, P., Roux, P., Kuperman, W.A. & Fehler, M.C., 2005. Surface wave tomography from microseisms in Southern California, *Geophys. Res. Lett.,* **32,** L14311.

Shapiro, N.M. & Ritzwoller, M.H., 2002. Monte-Carlo inversion for a global shear velocity model of the crust and upper mantle, *Geophys. J. Int.,* **151,** 88–105.

Shapiro, N.M., Ritzwoller, M.H., Molnar, P. & Levin, V., 2004. Thinning and flow of Tibetan crust constrained by seismic anisotropy, *Science,* **305,** 233–236.

Shapiro, N.M., Campillo, M., Stehly, L. & Ritzwoller, M.H., 2005. High-resolution surface wave tomography from ambient seismic noise, *Science,* **307,** 1615–1618.

Shen, W., Schulte-Pelkum, V. & Ritzwoller, M.H., 2011. A 3-D crustal and uppermost mantle model of the western US from receiver functions and surface wave dispersion derived from ambient noise and teleseismic earthquakes, 2011 Am. Geophys. Union Fall Meeting, Abstract S21B–2177.

Shui, T., 1988. Tectonic framework of the continental basement of southeast China. *Scientia Sinica,* **31**(B), 885–896.

Teng, J.W., Zhang, Z.J., Hu, J.F. & Wang, G.J., 2001. The 3-D structure of shear wave in South China and the southward extension of Tanlu fault, *Chi. Sci. Bull.,* **46**(4), 284–289.

Teng, J.W., Zeng, R.S., Yan, Y.F. & Zhang, H., 2003. Depth distribution of Moho and tectonic framework in eastern Asian continent and its adjacent ocean areas, *Sci China, Ser. D,* **46**(5), 428–446.

Villasenor, A., Ritzwoller, M.H., Levshin, A.L., Barmin, M.P., Engdahl, E.R., Spakman, W. & Trampert, J., 2001. Shear velocity structure of Central Eurasia from inversion of surface wave velocities, *Phys. Earth planet. Int.,* **123**(2–4), 169–184.

Wang Q. *et al*., 2001. Present-day deformation in China constrained by Global Positioning System Measurements, *Science,* **294,** 574–577.

Wang, Q. *et al*., 2005. Alkaline syenites in eastern Cathaysia (South China): link to Permian-Triassic transtension, *Earth. planet. Sci. Lett.,* **230,** 339–354.

Xu, J. & Guang, Z., 1994. Tectonic models of the Tan-Lu fault zone, Eastern China, *Int. Geol. Rev.,* **36,** 771–784.

Yang, Y. & Ritzwoller, M.H., 2008a. Teleseismic surface wave tomography in the western US using the Transportable Array component of USArray, *Geophys. Res. Lett.,* **5,** L04308, doi:10.1029/2007GL032278.

Yang, Y. & Ritzwoller, M.H., 2008b. The characteristics of ambient seismic noise as a source for surface wave tomography, *Geochem. Geophys. Geosys.,* **9**(2), Q02008, doi:10.1029/2007GC001814.

Yang, Y., Ritzwoller, M.H., Lin, F.-C., Moschetti, M.P. & Shapiro, N.M., 2008. The structure of the crust and uppermost mantle beneath the western US revealed by ambient noise and earthquake tomography, *J. geophys. Res.,* **113,** B12310.

Yang, Y. *et al*., 2010. Rayleigh wave phase velocity maps of Tibet and the surrounding regions from ambient seismic noise tomography, *Geochem. Geophys. Geosys.,* **11**(8), Q08010, doi:10.1029/2010GC003119.

Yang, Y., Ritzwoller, M.H., Zheng, Y., Levshin, A.L. & Xie, Z., 2012. A synoptic view of the distribution and connectivity of the mid-crustal low velocity zone beneath Tibet, *J. geophys. Res.,* in press, doi:10.1029/2011JB008810.

Yin, A., 2010. Cenozoic tectonic evolution of Asia: a preliminary synthesis, *Tectonophysics,* **288,** 293–325.

Zhang, P.Z., Deng, Q.D., Zhang, G.M., Ma, J., Gan, W.J., Min, W., Mao, F.Y. & Wang, Q., 2003. Active tectonic blocks and strong earthquakes in the continent of China, *Sci. China, Ser. D,* **46**(Supp.), 13–24.

Zhang, S.B., Zheng, Y.F., Wu, Y.B., Zhao, Z.F., Gao, S. & Wu, F.Y., 2006a. Zircon U–Pb age and Hf isotope evidence for 3.8 Ga crustal remnant and episodic reworking of Archean crust in South China, *Earth planet. Sci. Lett.,* **252,** 56–71, doi:10.1016/j.epsl.2006.09.027.

Zhang, S.B., Zheng, Y.F., Wu, Y.B., Zhao, Z.F., Gao, S. & Wu, F.Y., 2006b. Zircon isotope evidence for _3.5 Ga continental crust in the Yangtze craton of China, *Precambrian Res.,* **146,** 16–34.

Zhang, Z.M., Liou, J.G. & Coleman, R.G., 1984. An outline of the plate tectonics of China, *Geol. Soc. Am. Bull,* **95,** 295–312.

Zheng, J.P., Griffin, W.L., O'Reilly, S.Y., Zhang, M. & Pearson, N., 2006. Widespread Archean basement beneath the Yangtze Craton, *Geology,* **34,** 417–420.

Zheng, S., Sun, X., Song, X., Yang, Y. & Ritzwoller, M.H., 2008. Surface wave tomography of China from ambient seismic noise, *Geochem. Geophys. Geosyst.,* **9,** Q0502, doi:10.1029/2008GC001981.

Zheng, X.F., Yao, Z.X., Liang, J.H. & Zheng, J., 2010a. The role played and opportunities provided by IGP DMC of China National Seismic Network in Wenchuan earthquake disaster relief and researches, *Bull. Seism. Soc. Am.,* **100**(5B), 2866–2872.

Zheng, Y., Yang, Y., Ritzwoller, M.H., Zheng, X., Xiong, X. & Li, Z., 2010b. Crustal structure of the northeastern Tibetan Plateau, the Ordos Block, and the Sichuan Basin from ambient noise tomography, *Earthquake Sci.,* **3,** 465–476, doi:10.1007/s11589-010-0745-3.

Zheng, Y., Shen, W., Yang, Y., Xie, Z., Ritzwoller, M.H., 2011. Ambient noise Rayleigh wave tomography for northeast China, the Korean Peninsula, and the Sea of Japan, *J. geophys. Res.,* **116,** B12312, doi:10.1029/2011JB008637.

Zhou, X.M. & Li, W.X., 2000. Origin of late Mesozoic igneous rocks in southeastern China: Implications for lithosphere subduction and underplating of mafic magmas, *Tectonophysics,* **326,** 269–287, doi:10.1016/S0040-1951(00)00120-7.